Plasmons in topological insulator cylindrical nanowires

P. Iorio, C. A. Perroni, and V. Cataudella
CNR-SPIN and Physics Department "Ettore Pancini", Universita' degli Studi di Napoli "Federico II", Complesso Universitario Monte S. Angelo, Via Cintia, I-80126 Napoli, Italy
(Received 30 December 2016; published 12 June 2017)

We present a theoretical analysis of Dirac magnetoplasmons in topological insulator nanowires. We discuss a cylindrical geometry where Berry phase effects induce the opening of a gap at the neutrality point. By taking into account surface electron wave functions introduced in previous papers and within the random phase approximation, we provide an analytical form of the dynamic structure factor. Dispersions and spectral weights of Dirac plasmons are studied with varying the radius of the cylinder, the surface doping, and the strength of an external magnetic field. We show that, at zero surface doping, interband damped plasmonlike excitations form at the surface and survive at low electron surface dopings ($\sim 10^{10}$ cm^{-2}). Then, we point out that the plasmon excitations are sensitive to the Berry phase gap closure when an external magnetic field close to half quantum flux is introduced. Indeed, a well-defined magnetoplasmon peak is observed at lower energies upon the application of the magnetic field. Finally, the increase of the surface doping induces a crossover from damped interband to sharp intraband magnetoplasmons, which, as expected for large radii and dopings ($\sim 10^{12}$ cm^{-2}), approach the proper limit of a two-dimensional surface.

DOI: 10.1103/PhysRevB.95.235420

I. INTRODUCTION

Topological insulators (TI) are a new class of materials with many novel properties among which the bulk-boundary correspondence. In a three-dimensional TI, this correspondence leads to the formation of surface states protected from backscattering by time reversal symmetry that are observed in the gap of the bulk. The surface states connect the valence band with the conductive band through the formation of Dirac cones [1,2]. In the case of Bi_2Se_3, the electronic states are particularly simple since there is a single Dirac cone at Γ point of the Brillouin zone and a bulk gap around 0.5 eV [3–6].

Due to the sizable spin-orbit interaction characteristic of TI, spatial and spin degrees of freedom are strongly coupled and for a closed path, the electron spin acquires a π phase, known as Berry phase. In particular, this phase provides an antiperiodic boundary condition for the electron wave function after a 2π rotation. Therefore interesting situations take place when TI nanostructures, such as nanowires, are realized. For a TI nanowire, the Berry phase opens a small gap at the Γ point, hampering the formation of the Dirac cone and promoting the formation of different energy subbands corresponding to surface states [7–9]. The gap gets closed for a nanowire with an infinite cross-section or with a finite cross-section upon the application of magnetic field which reduces the effects of the Berry phase [10,11].

The collective plasmon excitations of Dirac electrons in TI have attracted a huge interest for their potential applications in terahertz detectors [12] and spintronic devices [13]. Only recently, Dirac magnetoplasmons were observed in TI showing high frequency tunability in the mid-infrared and terahertz spectral regions [14–18]. Due to the spin-momentum locking [19,20], these plasmons are always coupled to spin waves acquiring a spin character. For this reason, plasmons in TI are also called "spin-plasmons" [21–23]. From the experimental point of view, the observation of Dirac plasmons can be hampered by different effects: (i) they cannot be observed directly through an electromagnetic radiation because the moment conservation is prevented from their dispersion law; (ii) moreover, the existence of the impurities present in the material can make the contribution of the surface plasmons negligible compared to the bulk one [24]. In the former case, a solution can be obtained patterning the surface that add an extra-momentum contribution [25], while, in the latter case, a strategy to avoid the impurity problem is to make the ratio between volume and surface the lowest possible as in the case of nanostructures. This represents one of the reasons why Dirac electrons [26] and plasmons play an important role in nanostructures, such as nanowires [11,27,28] and nanoplates [29].

The random phase approximation (RPA) for the dielectric function has been used for gapped Dirac systems in different dimensions [30–32], but, as far as we know, not for the cylindrical nanowire geometry. In this work, we extend those studies to the case a cylinder exploiting the analytical electron wave functions that, in previous works [10,11], have been calculated for a TI cylindrical nanowire with a finite radius in the continuum limit. As part of this work, we analyze the system charge response considering the Coulomb interaction between electrons treating the interaction at the level of RPA. We provide an analytical solution of the inverse dielectric function, and, then, of the dynamic factor structure, relevant to study the response of the system to electronic scattering processes. The knowledge of these quantities in the limit of high surface density and infinite radius (two-dimensional surface) is used as a benchmark for the theoretical calculations.

The analysis starts from the case of zero surface doping, i.e., when the chemical potential is inside the small gap opened in the spectrum of the surface states by the effects of the Berry phase. In this case, it is possible to observe the dispersion of damped interband plasmonlike excitations that exhibits a minimum threshold value of the momentum along the cylinder axis. Very interesting results are obtained when an applied longitudinal magnetic field closes the gap

at half quantum flux and removes the degeneracy of the states by splitting the nanowire subbands. As an effect of this field, in the dynamic structure factor, we observe a well-defined magnetoplasmon peak with a long lifetime and an another excitation peak, resulting from the splitting of the same subband, at higher frequency and with lower spectral weight. When the chemical potential crosses the first subbands, it is possible to observe the existence of both damped interband and sharp intraband plasmon excitations with very different frequencies. With increasing the electron doping, the most important electronic excitations become those of intraband nature. Moreover, the increase of doping or of the cylinder radius induces a crossover to the two-dimensional regime where the effects of the magnetic field are no more relevant.

The paper is divided as follows. In Sec. II, a low-energy continuum model for a Bi_2Se_3 cylindrical nanowire is proposed; in Sec. III, an analytical form of the dynamic factor structure is provided; in Sec. IV, interband plasmonlike excitations are analyzed for zero surface doping; in Sec. V, the case of a finite surface doping is discussed; in Sec. VI, the features of inter and intraband plasmons are compared focusing on their different lifetimes. Details of the calculations are included in Appendices A and B.

II. THE MODEL

In this section, we recall the single-particle Hamiltonian model, its eigenvalues and eigenstates for a cylindrical wire, which represent the starting point for the calculation of the free electron charge susceptibility (or polarization function). Then, within the RPA approximation for the electron-electron Coulomb interaction, the dielectric function is obtained. In this section, we focus on the main results since more details of the calculations are provided in Appendices A and B.

As shown in Fig. 1(a), the wire is shaped as a very long cylinder with axis along z direction and radius R_0 in the x-y plane. Following the model proposed in previous works [10,11], the low-energy continuum model describing the electronic properties of Bi_2Se_3 close to the Γ point is given by the following three-dimensional Hamiltonian:

$$H(k) = M\,\mathbb{I}_2 \otimes \tau_z + C_1\,\sigma_z \otimes \tau_x k - iC_2[\sigma_x \otimes \tau_x(\partial_x + iA_x) + \sigma_y \otimes \tau_x(\partial_y + iA_y)]\,. \quad (1)$$

In Eq. (1), the operator $M = M_0 - M_2k^2 + M_2(\partial_x^2 + \partial_y^2)$ depends on the parameter M_0 controlling the bulk gap, and the parameter M_2 giving a mass correction. ∂_x and ∂_y are the partial derivatives along x and y, respectively, and having assumed the translational invariance along z direction, the quantity k represents the z axis conjugate momentum conserved by the Hamiltonian. The Pauli matrices σ_i, with $i = x, y, z$, describe the spin degrees of freedom, while the Pauli matrices τ_i, with $i = x,y,z$, take into account the two orbital degrees of freedom of the model. In Eq. (1), the symbol $\otimes$ represents the tensor product linking spin and orbital degrees of freedom. Finally, the parameters C_2 and C_1 control the interorbital and interspin couplings, while A_x and A_y are the x and y component, respectively, of the vector potential $\mathbf{A}$ corresponding to an homogeneous magnetic field $\mathbf{B}$ parallel to the axis of the cylinder.

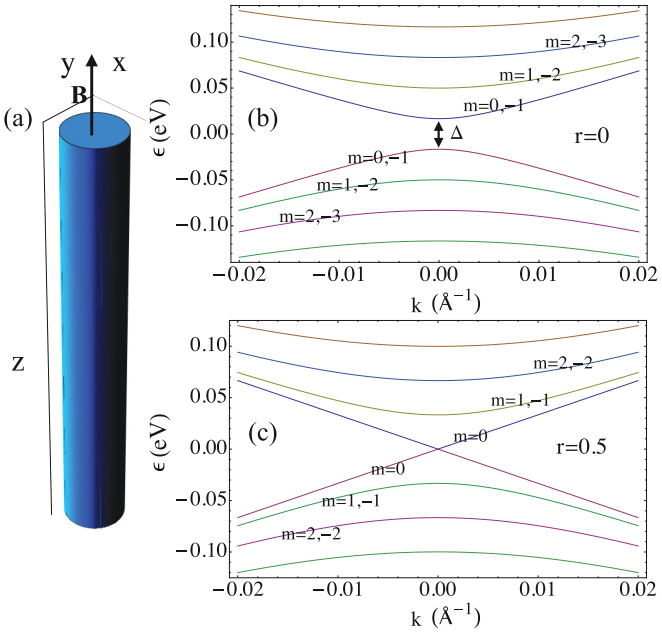

FIG. 1. (a) Sketch of the cylindrical wire with translational invariance along z direction in the presence of a magnetic field $\mathbf{B}$ parallel to the z axis. (b) The energy dispersion (in units of eV) as a function of momentum k (in units of Å^{-1}) along z direction with the formation of a gap Δ and the presence of subbands for $r = 0$. (c) The energy dispersion (in units of eV) as a function of momentum k (in units of Å^{-1}) along z direction with the closure of the gap for $r = 0.5$ (half quantum flux). The surface state spectrum is obtained for a cylindrical wire with a radius $R_0 = 100$ Å.

In the absence of magnetic field, the Hamiltonian is represented by the following matrix operator:

$$H(k) = \begin{bmatrix} M & C_2k & 0 & -iC_1\partial_- \\ C_2k & -M & -iC_1\partial_- & 0 \\ 0 & -iC_1\partial_+ & M & -C_2k \\ -iC_1\partial_+ & 0 & -C_2k & -M \end{bmatrix}, \quad (2)$$

with the derivative operator $\partial_\pm = \partial_x \pm i\partial_y$. The following parameters for Bi_2Se_3 are used in this paper [6,11]: $M_0 = -0.28$ eV, $M_2 = 40.00$ eV Å^2 and $C_1 = C_2 = C = 3.33$ eV Å. The bulk gap is a few tenths of eV, being proportional to M_0. The choice $C_1 = C_2$ ensures that the model has particle-hole (p-h) symmetry.

The single-particle energies and states of the Hamiltonian (1) can be analytically derived for a cylinder with a large radius [see Fig. 1(a) for a sketch of the system] by using the cylindrical coordinates (ρ,ϕ,z) for the electron position $\vec{r}$ [10,11]. We have shown in a previous paper [11] that, in a cylinder with a radius R_0 larger than 100 Å, the surface eigenvalues ϵ_α and eigenfunctions $\psi_\alpha(\rho,\phi,z)$ of Eq. (1) can be very accurately expressed in the following form:

$$\epsilon_\alpha = \epsilon^s_{k,m} = sC_2\sqrt{k^2 + (1 + 2m - 2r)^2\tilde{\Delta}^2(R_0)}, \quad (3)$$

and

$$\psi_\alpha(\rho,\phi,z) = \psi^s_{k,m}(\rho,\phi,z) = \sqrt{\frac{1}{4\pi L}} e^{ikz} R(\rho) e^{im\phi} \mathbf{u}^s_{k,m}(\phi). \quad (4)$$

In Eqs. (3) and (4), the eigenvalue and eigenstate label is indicated by $\alpha = (k,m,s)$, where the relative number m is related to the symmetry of the cylindrical confinement and $s = \pm$. The effects of a longitudinal magnetic field are included in Eq. (3) through the parameter r, which is equal to the ratio between the magnetic flux Φ threaded by the cylinder and the quantum flux $\Phi_0 = \hbar/2e$: $r = \Phi/\Phi_0$.

As reported in Eq. (3), a gap $\Delta(R_0) = 2C_2\tilde{\Delta}(R_0)$, with $\tilde{\Delta}(R_0) = C_1/(2C_2R_0)$, opens at $k = 0$ in the spectrum of the surface states for $r = 0$ (absence of the magnetic field). For a radius $R = 500$ Å according to the model parameters considered in in this paper, the surface states have a gap $\Delta = 6.66$ meV, which is much smaller than the bulk gap. The extra term responsible for the nanowire gap even for $m = 0$ is a direct consequence of the Berry phase. As shown in Fig. 1(b), for $r = 0$, above and below the semigap, the spectrum shows different subbands depending on the quantum number m. Furthermore for both positive and negative energies, the subbands are twofold degenerate in m. For example, in Eq. (3) for $r = 0$, the couple $m = 0, m = -1$ corresponds to the same energy.

We stress that the case of a wire is quite different from that of a slab. In fact, in the second case, the gap of the system depends only on the thickness of the slab. When the slab is few tens of angstrom thick, the surface states of the two faces interfere with each other opening a gap [33]. If the thickness is about 70 Å, the Dirac cone is restored closing the gap. A different situation occurs when, regardless of the mutual distance, the two surfaces are always connected to each other, creating a closed loop, as in the case of the wire cross-section. In fact, in this case, we can imagine in a naive way that surface states always communicate with each other (quantum interference effects) through a purely geometric phase, the Berry phase. As a consequence, the opening of a small gap at the Γ point occurs even for large nanowire cross-sections. For the radius considered in this paper, from 500 to 4000 Å, the opening of the gap is purely a consequence of the Berry phase, and it cannot be ascribed, for example, to the superposition of states on opposite sides of a cylinder diameter.

In the presence of a longitudinal magnetic field, the gap Δ gets reduced and the twofold degeneracy in m removed. Actually, interference terms due to magnetic field weaken the effects of the Berry phase. In particular, in the case of $r = 0.5$ (half quantum flux), a total cancellation of the Berry phase effects takes place because of the magnetic field even for a finite radius nanowire. For $r = 0.5$, as reported in Eq. (3), the $m = 0$ subband shows no more gap. As shown in Fig. 1(c), in the case of $r = 0.5$, a twofold degeneracy is again restored even if it has a different character. For example, in contrast with the case of $r = 0$, $m = 1$, $m = -1$ are degenerate for $r = 0.5$.

In Eq. (4), L is the length of the cylinder along the z axis, $R(\rho)$ is the radial function different from zero for $0 < \rho < R_0$, $\mathbf{u}^s_{k,m}(\phi)$ is a quadrispinor depending on the angular variable ϕ [see Appendix A for details about the function $R(\rho)$ and the four components of $\mathbf{u}^s_{k,m}(\phi)$]. In the limit of a large radius R_0, the radial function $R(\rho)$ for the surface states is essentially localized for values of ρ close to R_0.

Using surface single-particle energies and states labeled by α, one can calculate the free electron susceptibility $\chi(\vec{r},\vec{r}';\omega)$ (or polarization function) at zero temperature:

$$\chi(\vec{r},\vec{r}';\omega) = \sum_{\alpha,\alpha'} \frac{f(\epsilon_{\alpha'}) - f(\epsilon_\alpha)}{\epsilon_{\alpha'} - \epsilon_\alpha + \hbar(\omega + i0^+)} \times \psi^*_{\alpha'}(\vec{r})\psi_\alpha(\vec{r})\psi^*_\alpha(\vec{r}')\psi_{\alpha'}(\vec{r}'), \quad (5)$$

where $f(\epsilon_\alpha)$ is the Fermi function at zero temperature calculated at the energy ϵ_α, which is related to the chemical potential μ. In the case of the TI nanowire, we use the eigenvalues (3) and the corresponding eigenfunctions (4) in cylindrical coordinates. Hence, in Eq. (5), $\alpha = (k,m,s = \pm)$, $\alpha' = (k + q, m + l, s' = \mp)$, where q is the transferred momentum along z axis, l is the relative number linking the subband m to the subband $m' = m + l$. Indeed, m and $m' = m + l$ are the variables conjugate to ϕ and ϕ', respectively. The susceptibility for the cylinder becomes

$$\chi(\vec{r},\vec{r}';\omega) = \chi(\rho,\rho',z - z',\phi - \phi';\omega) = R^2(\rho)R^2(\rho')\chi_0(z - z',\phi - \phi';\omega), \quad (6)$$

where $\chi_0(z - z',\phi - \phi';\omega)$ reflects the translation invariance along z axis and the rotation invariance around z axis due to the cylindrical geometry (details about $\chi_0(z - z',\phi - \phi';\omega)$ are provided in Appendix A. Clearly, the susceptibility is different from zero for values of the positions $\vec{r}$ and $\vec{r}'$ inside the cylinder. We point out that, along the radial direction, the susceptibility depends on the product of the squares of the radial functions calculated in ρ and ρ', respectively. This separation of the radial dependencies will be of paramount importance for the calculation of the inverse of the dielectric function.

Finally, we calculate the dielectric function due to the surface charges of the TI cylindrical wire within the RPA approximation for the electron-electron Coulomb interaction. Even if we confine electrons within the cylinder, the generated electromagnetic fields affects all the space and, therefore, the dielectric function is defined also outside the cylinder. Within the RPA approximation, the dielectric constant $\epsilon(\vec{r},\vec{r}';\omega)$ is defined in the following way:

$$\epsilon(\vec{r},\vec{r}';\omega) = \delta(\vec{r} - \vec{r}') - \int d\vec{r}_1 V(\vec{r} - \vec{r}_1)\chi(\vec{r}_1,\vec{r}';\omega), \quad (7)$$

where $V(\vec{r} - \vec{r}_1) = e^2/|\vec{r} - \vec{r}_1|$ is the Coulomb potential in real space and the integration is over the volume enclosed by the cylinder [34]. We emphasize again that $\vec{r}$ can assume values both inside and outside the cylinder unlike $\vec{r}_1$ and $\vec{r}'$. In the next section, we will see that, in order to describe the response of the system to external probes, we need to calculate the inverse of the dielectric function $\epsilon^{-1}(\vec{r},\vec{r}';\omega)$. As discussed in Appendix B, in order to make the inversion of the dielectric function in Eq. (7), we solve analytically an integral equation with a separable variable kernel.

III. DYNAMIC STRUCTURE FACTOR

In this section, we provide an analytic form of the dynamic structure factor for a TI cylindrical wire. This quantity is relevant for example in electron-energy-loss experiments (EELS), where an electron impinges on the sample and loses energy by exciting plasmons. This energy loss is given by the imaginary part of the integral of the potential created by the electron, and the induced charge [35]. When the potential due to an electron is taken proportional to a plane wave, one can calculate the response function $L(\vec{q};\omega)$ making a double Fourier transform of the inverse dielectric function:

$$L(\vec{q};\omega) = -\mathrm{Im}\left[\frac{1}{V}\iint d\vec{r}d\vec{r}'\epsilon^{-1}(\vec{r},\vec{r}';\omega)e^{-i\vec{q}\cdot\vec{r}}e^{i\vec{q}\cdot\vec{r}'}\right], \tag{8}$$

where V is the volume enclosed by the cylinder and the two integrals are over all the space. It can be shown that the response function $L(\vec{q};\omega)$ in Eq. (8) is proportional to the dynamic structure factor [36], whose peaks characterize the electronic excitations, such as plasmons, induced by scattering processes. Since the system has translational invariance in the z direction and rotational invariance around z axis, as discussed in Appendix B, one can use partial Fourier transforms in q and l for the Coulomb potential $V(\vec{r}-\vec{r}_1)$ and the polarization function $\chi(\vec{r}_1,\vec{r}')$ obtaining the following result:

$$\begin{aligned} &L(q,|\mathbf{q}_{||}|;\omega) \\ &= -\frac{2}{R_0^2}\mathrm{Im}\left[\sum_l \frac{\chi_0(q,l;\omega)}{1-\chi_0(q,l;\omega)\tilde{V}_{q,l}}\right. \\ &\left.\times \int_0^{R_0} d\rho'\rho' \mathrm{J}_l(|\mathbf{q}_{||}|\rho')R(\rho')^2 \int_0^{\infty} d\rho\rho\, \mathrm{J}_l(|\mathbf{q}_{||}|\rho)S_{q,l}(\rho)\right]. \end{aligned} \tag{9}$$

where $|\mathbf{q}_{||}|$ is the modulus of the momentum transverse to the axis z of the cylinder (parallel to the $x-y$ plane), and J_l are the Bessel functions of the first kind. In Eq. (9), $\tilde{V}_{q,l}$ takes into account the Coulomb repulsion:

$$\tilde{V}_{q,l} = 4\pi \int d\rho\rho R^2(\rho)S_{q,l}(\rho), \tag{10}$$

since $S_{q,l}(\rho)$ is defined as

$$S_{q,l}(\rho) = e^2 \int d\rho'\rho' R^2(\rho')I_l(|q|\rho_<)K_l(|q|\rho_>), \tag{11}$$

with I_l and K_l the modified Bessel functions of the first and second kind, respectively. In Appendix A, we report the expansion of the Coulomb potential in cylindrical coordinates clarifying that $\rho_<$ and $\rho_>$ appearing in Eq. (11) represent the smaller and larger of ρ and ρ', respectively.

The zeros of the denominator in equation (9) provide the plasmon dispersions. Indeed, one has the equation

$$1-\chi_0(q,l;\omega)\tilde{V}_{q,l} = 0 \tag{12}$$

typical of the RPA approach. In this paper, we focus on the contributions for $|\mathbf{q}_{||}| \to 0$, therefore we consider probes propagating parallel to the axis of the cylinder. This means that we only have to analyze the term $L(q,0;\omega)$ corresponding to $l=0$:

$$L(q,0;\omega) = -\frac{2}{R_0^2}\mathrm{Im}\left[\frac{\chi_0(q,0;\omega)}{1-\chi_0(q,0;\omega)\tilde{V}_{q,0}}\int_0^{\infty} d\rho\rho\, S_{q,0}(\rho)\right]. \tag{13}$$

In the limit of large radius R_0 and small q, it is possible to show how the potential $R_0\tilde{V}_{q,0}$ converges to the two-dimensional Coulomb potential $V_q^{2D} = 2\pi e^2/q$. As reported in Appendix A, in the limit of infinite radius, the dynamic polarization $\chi_0(q,0;\omega)$ also converges to that of the two-dimensional case [32].

In addition to the plasmon frequencies and their spectral weights, we can also calculate the induced charge density $d(\vec{r})$, potential $\Phi(\vec{r})$ and electric field $\vec{E}(\vec{r})$ corresponding to these modes. In Appendix A, we provide the analytical expressions of these quantities and all the details of the calculations. We show that the electronic charge density corresponding to a mode at fixed q and l is

$$d(\vec{r}) = d(\rho,\phi,z) = e^{iqz}e^{il\phi}B_{q,l}(R_0)R^2(\rho), \tag{14}$$

where the dependence on ρ is only through the square of the radial function $R(\rho)$, and $B_{q,l}(R_0)$ is an arbitrary constant depending in general also on the cylinder radius R_0. As shown in Appendix A, through the density, one can calculate the electric potential Φ relative to a mode at fixed q and l:

$$\begin{aligned} \Phi(\vec{r}) = \Phi(\rho,\phi,z) &= e^{iqz}e^{il\phi}B_{q,l}(R_0) \\ &\times \int_0^{R_0} d\rho'\rho' R^2(\rho')K_l(q\rho_>)I_l(q\rho_<). \end{aligned} \tag{15}$$

Through the potential, one can determine the electric field $\vec{E}(\vec{r}) = -\nabla\Phi(\vec{r})$ inside ($\rho < R_0$) and outside ($\rho > R_0$) the cylinder. In principle, all the three components exist: radial E_ρ, longitudinal E_z, and angular E_ϕ. We note immediately that if we take only the modes at $l=0$, the dependence on the angular part disappears in Eq. (15). Therefore, for the modes at $l=0$, there are only longitudinal and transverse components of the field, while, for modes with l different from zero, also the angular component E_ϕ appears. As discussed in Appendix A, the electric field for $l=0$ is similar to that of the TM mode at $l=0$ in the case of surface plasmons for conventional metallic cylinders [37]. In this paper, we analyze the electrostatic limit, where the magnetic field is always assumed zero. Therefore the axial component of the magnetic field is clearly zero for the TM mode at $l=0$. We recall that, in TI, Hall currents can lead to a magnetoelectric effect according to which a magnetic field can induce a charge polarization. As a consequence, the separation between TE and TM is not exact in TI cylinders for l=0 [38,39]. However, the magnetoelectric effect can be treated at a perturbative level and have practically no impact on the plasmon properties of TI systems. We remark that, within the electrostatic limit adopted in this paper, these very weak effects on the plasmon are automatically neglected.

As discussed in Appendix A, for the radii chosen in this paper ($R_0 \geqslant 500$ Å), the induced density becomes practically different from zero only on the lateral surface of the cylinder. For the modes with $l=0$, we can provide analytical

expressions for the electric field:

$$(E_\rho, E_z) = B_{q,l=0}(R_0)\begin{cases}(q\,I_1(q\rho)K_0(q\,R_0)e^{iqz},\ iq\,I_0(q\rho)K_0(q\,R_0)e^{iqz}), & \rho \leqslant R_0,\\ (-q\,K_1(q\rho)I_0(q\,R_0)e^{iqz}, iq\,K_0(q\rho)I_0(q\,R_0)e^{iqz}), & \rho > R_0.\end{cases} \tag{16}$$

Inside the cylinder ($\rho < R_0$), the radial component E_ρ goes as $I_1(qr)$, therefore, at finite q, E_ρ is proportional to $q\rho$ for very small values of ρ. On the other hand, outside the cylinder ($\rho > R_0$), E_ρ goes as $K_1(q\rho)$, therefore, at finite q, E_ρ is proportional to $e^{-q\rho}/\sqrt{q\rho}$ for very large values of ρ. Moreover, as expected, for $q \to 0$, the electric field inside the cylinder is zero, while, outside the cylinder, the longitudinal component E_z vanishes, and the radial component E_ρ goes as $1/\rho$. It is apparent that the long-range spatial variation of the electric field is completely different from that of the charge density which is essentially localized on the lateral surface of the cylinder.

For a system with p-h symmetry, $\chi_0(q,l;\omega) = \chi_0(q,l;-\omega)^*$. Therefore the results will be given only for chemical potential $\mu > 0$, $\omega > 0$, and $q > 0$. Furthermore, since we will consider only the $l = 0$ contribution, in the following, we name $\tilde{V}_{q,0} = \tilde{V}_q$ and $\chi_0(q,0;\omega) = \chi_0(q;\omega)$. As shown in Appendix A and following what is done in literature, we can divide the polarization function for massive Dirac electrons into three contributions:

$$\chi(q;\omega) = -\chi_\infty^-(q;\omega) + \chi_\mu^-(q;\omega) + \chi_\mu^+(q;\omega), \tag{17}$$

where the subscripts are related to the position of the chemical potential: $-\chi_\infty^-(q;\omega)$ is the contribution for $\mu < \Delta$, $\chi_\mu^-(q;\omega) + \chi_\mu^+(q;\omega)$ is the additional contribution for $\mu > \Delta$. In Eq. (17), the superscript $+$ indicates intraband transitions, while the superscript $-$ interband transitions. Therefore one can define

$$\chi_T^\pm(q;\omega) = \frac{1}{4C_2\pi^2}\sum_m \int_{-T}^{T} dk\left[1 \pm \frac{k(k+q) + \tilde{\Delta}_m^2(R_0)}{\tilde{\epsilon}_{k,m}\tilde{\epsilon}_{k+q,m}}\right] \times \left[\frac{\tilde{\epsilon}_{k,m} \mp \tilde{\epsilon}_{k+q,m}}{(\tilde{\omega}+i\tilde{\eta})^2 - (\tilde{\epsilon}_{k,m} \mp \tilde{\epsilon}_{k+q,m})^2}\right], \tag{18}$$

with $\tilde{\Delta}_m(R_0) = \tilde{\Delta}(R_0)(1+2m-2r)$, $\tilde{\omega} = \hbar\omega/C_2$, $\tilde{\epsilon}_{k,m} = \epsilon_{k,m}/C_2$, $\tilde{\mu} = \mu/C_2$, and $\tilde{\eta} = \eta/C_2$, with η very small positive energy. The integration limit T is equal to infinity for μ in gap, while $T = \sqrt{\tilde{\mu}^2 - (1+2m-2r)^2\tilde{\Delta}^2}$ otherwise. The sum over m for the case $\mu < \Delta$ has to be made over all subbands, then m goes from minus infinity to infinity. On the other hand, for $\mu > \Delta$, the sum is limited by the condition of existence of T, that is, $\tilde{\mu}^2 - \tilde{\Delta}^2(1+2m-2r)^2 > 0$, with m integer.

IV. ZERO SURFACE DOPING

In a previous section, we have pointed out that the effect of the Berry phase is to open a small gap in the energy spectrum. In this section, we provide a description of the interband surface excitations, when the chemical potential μ is in the Berry phase gap. This means that the chemical potential is in the middle of the gap: $\mu = 0$ (due to the p-h symmetry). As shown in Fig. 1, the basic p-h excitations are due to transitions from states with negative energies [$s = -$ in Eq. (3)] to those with positive energies [$s = +$ in Eq. (3)].

As discussed in this section, in the absence of an applied magnetic field, the interband excitations are severely damped. Moreover, these interband excitations are not present in the limit $q \to 0$. For this reason, we call the interband mode a plasmonlike excitation. This will help comparing this excitation with the sharp intraband mode which is well-defined in the limit $q \to 0$. In the following, the intraband mode will be called intraband plasmon. In the next two sections, we will analyze the features of interband and intraband excitations, respectively. In Sec. VI, the short lifetimes of interband plasmonlike excitations will be compared with long ones of intraband plasmons.

In this section, considering the chemical potential in gap ($\mu = 0 < \Delta$), we need only to analyze the contribution $-\chi_\infty^-$ of the equation (17). Moreover, the $l = 0$ contribution to the susceptibility come only from interband transitions associated to the same subband number m but opposite s in Eq. (3) (see for clarity also Fig. 1).

We determine the plasmon dispersion from Eq. (12) considering $l = 0$:

$$1 - \mathbb{R}\mathrm{e}[\chi_0(q;\omega)]\tilde{V}_q = 0. \tag{19}$$

We solve numerically equation (19) taking η [see Eq. (18)] very small but finite. As shown in an example in Fig. 2), the equation has more solutions corresponding to different frequencies, all with a finite imaginary part. Furthermore, for each value of R_0, these interband plasmonlike excitations show a minimum frequency related to the finite gap $\Delta(R_0)$. In fact, the real part $\mathrm{Re}(-\chi_\infty^-)$ is completely negative for

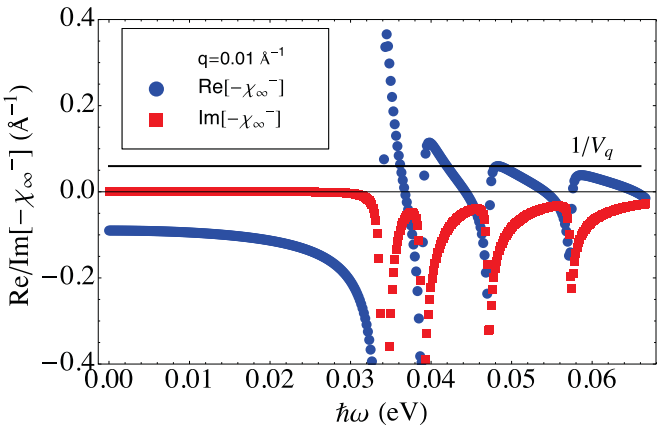

FIG. 2. Real (blue circles) and imaginary (red squares) part of the susceptibility (in units of Å^{-1}, obtained numerically with $\eta = 1.5 \times 10^{-4}$ eV) as a function of the energy (in units of eV) for $q = 0.01$ Å^{-1} at $R_0 = 500$ Å and $r = 0$. Large variations of the real part are related to those of the imaginary part in correspondence with the same value of $\hbar\omega = C_2\sqrt{q^2 + 4\tilde{\Delta}^2(1+2m-2r)^2}$ at $r = 0$. The intersections that $1/\tilde{V}_q$ (black line) has with $\mathrm{Re}(-\chi_\infty^-)$ give the plasmon frequencies.

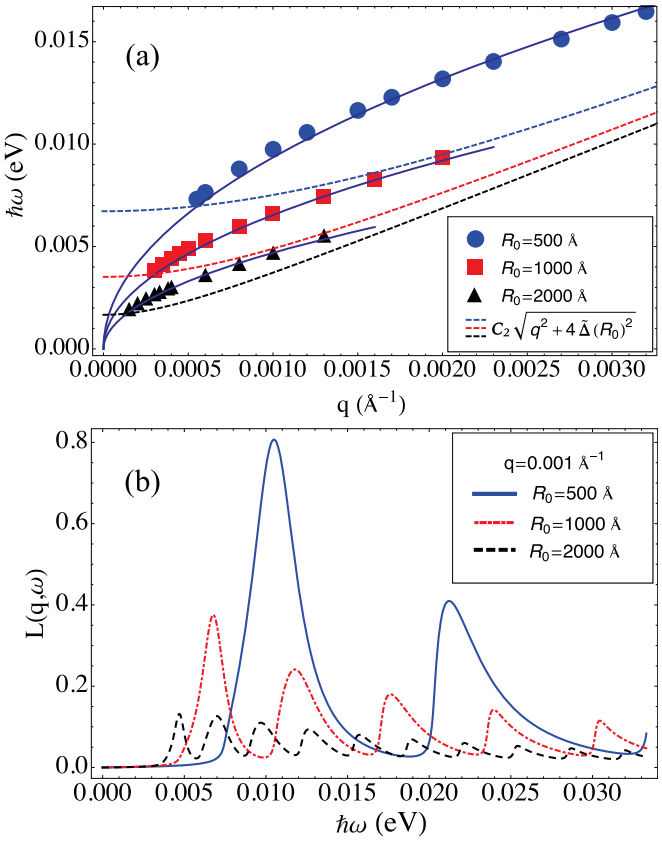

FIG. 3. (a) Interband plasmonlike dispersion (in units of eV) as a function of the wave vector q (in units of Å^{-1}) for different values of the cylinder radius. Plasmon excitations are present only for energies larger than $C_2\sqrt{q^2+4\tilde{\Delta}^2(R_0)}$. The fits (continuous lines) of the dispersions indicate that, above the minimum q, the dispersion is square-root-like: $\hbar\omega = \alpha\sqrt{q}$. For $R_0 = 500$ Å $\alpha \sim 0.3$ eV Å$^{1/2}$; for $R_0 = 1000$ Å, $\alpha \sim 0.2$ eV Å$^{1/2}$; for $R_0 = 2000$ Å, $\alpha \sim 0.155$ eV Å$^{1/2}$. (b) The dynamic structure factor $L(q;\omega)$ as a function of the energy (in units of eV) at $q = 0.001$ Å^{-1} for different values of the cylinder radius.

$\hbar\omega < C_2\sqrt{q^2+4\tilde{\Delta}^2(R_0)}$, instead it assumes also positive values for larger values of frequency. Since the solutions of the equation (19) exist only for values of $\mathrm{Re}(-\chi_\infty^-) > 0$, plasmon dispersion exists only above the curve $\hbar\omega = C_2\sqrt{q^2+4\tilde{\Delta}^2(R_0)}$. In Fig. 3(a), we report these curves for different cylinder radii.

Associated with minimum frequency ω, there is also a minimum momentum q_t for which equation (19) admits a solution. This is clearly shown in Fig. 3(a). With decreasing the radius R_0, the gap $\Delta(R_0)$ gets enhanced, therefore this minimum q_t becomes bigger. It is worthwhile noting that, due to the existence of a minimum threshold q_t, it is not possible to derive an analytical expression of the dispersion in the limit of small q, as in the case of intraband plasmons. In Fig. 3(a), we report our numerical analysis for the plasmon dispersions at different cylinder radii.

It is important to analyze the behavior of the potential $\tilde{V}_q$ in the limit of small q, since two different regimes are present:

$$\tilde{V}_q \sim \begin{cases} e^2 K_0(qR_0) \mapsto -e^2 \log(qR_0), & q \ll 1/R_0, \\ e^2/(qR_0) = V_q^{2D}/R_0, & q > 1/R_0. \end{cases} \quad (20)$$

Indeed, for $q \ll 1/R_0$, $\tilde{V}_q$ shows a one-dimensional type behavior, while, for $q > 1/R_0$ it is more two-dimensional [30].

Interband plasmonlike excitations are stable only for $q > q_t$, which is comparable with $1/R_0$ in the absence of the magnetic field. Therefore, as shown in Fig. 3(a), the plasmon dispersion is similar to the two-dimensional case ($\omega \sim \sqrt{q}$). Moreover, we observe that, for larger values of q, the dispersion tends towards $C_2 q$. For the radii considered in this paper, the linear regime is reached at most at $q > 0.01$ Å^{-1}. This value of q is in any case smaller than 0.1 Å^{-1}, which represents the order of magnitude of the wave vector at the border of the Brillouin zone in materials like Bi_2Se_3. Therefore the analysis pursued in this paper considers values of the wave vector q where RPA is known to give a reliable description of the electronic excitations. The dynamic structure factor calculated in Eq. (13) provides the spectral weights associated with the plasmon frequencies. As shown in Fig. 3(b), this allows us to estimate the damping of the plasmon and its lifetime. In the case of interband plasmonlike excitation studied in this section, we stress that, for long wavelength, only the first peak corresponds to a solution of Eq. (19). The peaks at higher frequencies are associated to minima of the right side member of Eq. (19), and correspond to higher values of the subband number m. Actually, we notice that only the first peak has a Lorentzian shape while the others become progressively more asymmetric with increasing the frequency. As shown in Fig. 3(b), for the radius $R_0 = 500$ Å the first plasmon peak almost saturates the spectral weight, while, for the radius $R_0 = 2000$ Å it has a spectral weight comparable with high frequency peaks. In any case, the increase of the radius R_0 induces a decrease of the spectral weight as we see in Fig. 3(b) and a shift of the plasmon frequency toward lower values. If one further increases the value of R_0, the spectral weight of the interband plasmon frequency falls to zero. Indeed, as discussed in Appendix A, for $R_0 \to \infty$, one reaches, as expected, the two-dimensional limit where interband plasmonlike excitations are no more present. A similar decrease of the plasmon spectral weight is observed when wave vector q increases.

The application of a magnetic field along the axis of the cylindrical wire introduces a magnetic flux Φ which changes the gap value through the term $r = \Phi/\Phi_0$ present in Eq. (3). This way, it is possible to study the effects of the Berry phase on Dirac interband plasmon frequencies in nanowires up to the closing of the gap. As shown in Fig. 1, the additional effect of the magnetic field is to remove the degeneracy of energy states and it has an interesting effect on the dynamic structure factor. In fact, the presence of the magnetic field separates a peak into two: one at a frequency lower and the other at a frequency larger than the peak at $r = 0$, as shown in Fig. 4(a).

We notice that the sum of the spectral weights of two new plasmon peaks is similar to that of the main peak for zero magnetic field. The redistribution of this weight is not homogeneous, indeed, almost all the contribution is given by

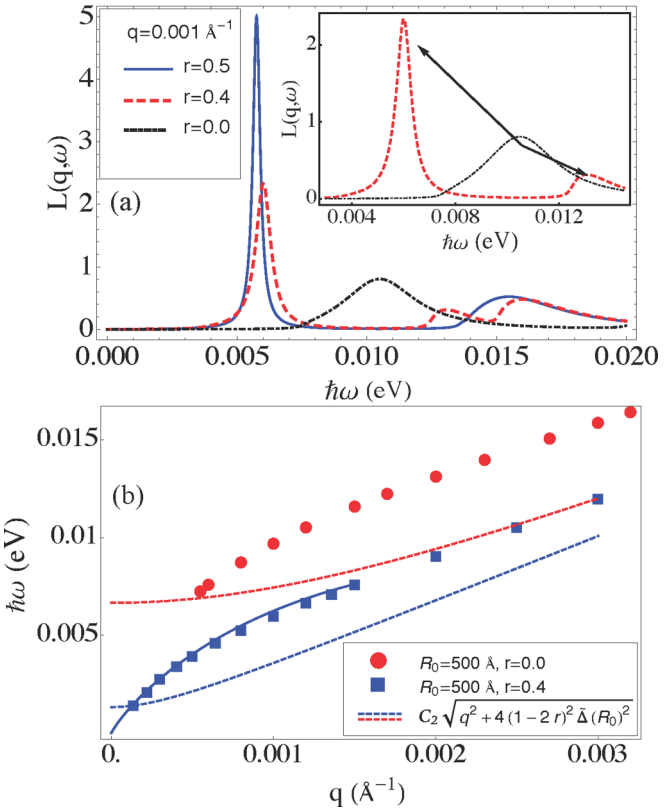

FIG. 4. (a) The dynamic structure factor as a function of the energy (in units of eV) at $R_0 = 500$ Å and $q = 0.001$ Å^{-1} for some values of the ratio of the magnetic fluxes. Note the separation of the plasmon peak into two peaks (shown in the inset by the arrows). (b) Plasmon dispersion (in units of eV) as a function of the momentum q (in units of Å^{-1}) at $R_0 = 500$ Å for two values of r: $r = 0$ (red circles) and $r = 0.4$ (blue squares). Plasmon excitations are present only for energies larger than $C_2\sqrt{q^2 + 4(1-2r)^2\tilde{\Delta}^2(R_0)}$. The fit (continuous line) of the $r = 0.4$ curve provides a dispersion typical of a one-dimensional system: $\hbar\omega = \alpha q\sqrt{K_0(qR_0)}$, with $\alpha = 6.5$ eV Å^{-1}.

the low-frequency peak, as we show in the inset of Fig. 4(a). Not only the integral of this peak is more important but also the peak itself is better defined being narrower and higher. Indeed, the closure of the Berry gap caused by the magnetic field gives rise to a magnetoplasmon with a very long lifetime, therefore more likely to be observed experimentally. Our analysis suggests that, in the presence of a magnetic field, the magnetoplasmon peak should be observed at lower frequency. Furthermore, for a magnetic field near half quantum flux, as shown in Fig. 4(b) for $r = 0.4$, when the gap is practically closed, the minimum threshold q_t becomes very close to zero. As discussed in Eq. (20), the potential for values of $q \ll 1/R_0$ has a one-dimensional behavior, and, therefore, also the magnetoplasmon for wavelength $q_t < q \ll 1/R_0$ acquires a dispersion typical of one-dimensional systems: $\omega \propto q\sqrt{K_0(qR_0)}$, as shown in Fig. 4(b). Unlike the case without magnetic field, a threshold minimum q_t tending to zero with the closing of the gap allows us to explore the region which has a one-dimensional character. Finally, with the closing of the gap *at* $r = 0.5$, we restore the degeneration in the subbands but the resulting excitations are at frequencies

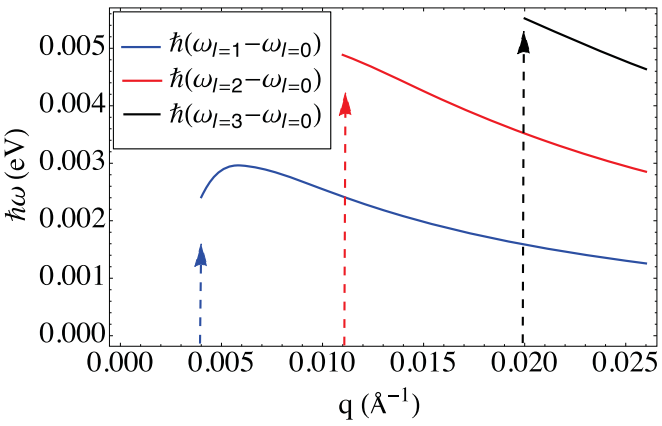

FIG. 5. Differences of the frequencies (in units of eV) at $l = \pm 1$, ± 2, and ± 3, respectively, with that at $l = 0$ as a function of the wave vector q (in units of Å^{-1}) for a radius $R_0 = 500$ Å in the case of zero surface doping. The dashed arrows indicate the different minimum thresholds q_t for $l = \pm 1$, ± 2, and ± 3, respectively.

lower than those for zero magnetic field. Indeed, the resulting peak of the dynamic structure factor has a similar spectral weight but it is much higher and narrower. We will see in the next section that the nature of this magnetoplasmon at zero gap is different from that of interband type since it is similar to an intraband plasmon.

Up to now, the entire analysis for interband plasmonlike excitation has been made for the mode at $l = 0$. However, Eqs. (9) and (12) depend on a generic relative number l. Through the dynamic structure factor, a spectral weight can be associated with each zero of the RPA equation in (12) for different l. A finite value of l means selecting different transitions between the subbands shown in Fig. 1. In fact, for example, $l = \pm 1$ means going from subband m to subband $m \pm 1$. We derive the plasmon dispersion at zero doping for $l = \pm 1$, ± 2, and finally ± 3 and, as shown in Fig. 5, we study the difference of the plasmon frequencies at finite l with respect to the frequencies at $l = 0$. Of course, we find the same zero for opposite values of l. That is why in Fig. 5 we report only positive values of l. The three dispersions are very close in frequency and have the same monotony, but, with the increase of the parameter l, also the minimum threshold q_t (indicated by the dashed arrows in Fig. 5) gets significantly enhanced. This is an expected result since a greater l involves higher energy transitions. Therefore the required q_t must be higher and comparable to the minimum difference energy between subbands.

For the solutions found in Fig. 5, we can evaluate the spectral weight through the dynamic structure factor of Eq. (9). Only for the conjugate variable $q_{||} \neq 0$, values of l different from zero can be considered. If one chooses small values of $q_{||}$, the momentum appears practically parallel to the axis of the cylinder. In particular, for each value of q, we have considered a $q_{||}$ about an order of magnitude lower. The result is that, with increasing l, the spectral weight decreases significantly, confirming that the contribution for the mode at $l = 0$ is the most important. In fact, already for $l = 3$, the spectral weight can be considered practically equal zero being three orders of magnitude smaller than that at $l = 0$.

V. FINITE SURFACE DOPING

In this section, we analyze the case of finite surface electron doping: $\mu > \Delta$. In order to find the dispersion and spectral weight associated with the plasmon excitations, we have to consider all three contributions of Eq. (17). We start analyzing the case of low electron doping to understand how the crossover between inter and intraband plasmon takes place.

We define the electron doping for the case of a cylindrical wire as follows:

$$n = \frac{1}{2\pi^2 R_0} \sum_{m=-M+1}^{M-1} \sqrt{\tilde{\mu}^2 - (1+2m-2r)^2 \tilde{\Delta}^2}, \qquad (21)$$

where M is the number of the subbands intersected by chemical potential. We choose to study the case in which the potential intersects a single subband equivalent to $m = 0$. For this condition, we have an electron doping equal to $n = 10^{10}\ \mathrm{cm}^{-2}$. This way, Eq. (19) always admits a solution for each value of momentum q due to the intraband contribution given by $\chi_\mu^+(q;\omega)$, unlike the case of $\mu = 0$ studied in the previous section where there was a minimum threshold q_t. For this reason, it is possible to make the $q \to 0$ limit for the polarization function valid at each ω:

$$\chi_0(q \to 0;\omega) = \frac{1}{2\pi^2 C_2} \sum_m \frac{k_F(m)\ \tilde{\mu}\ q^2}{\tilde{\mu}\ \omega^2 - k_F(m)\ q^2}, \qquad (22)$$

where $k_F(m) = \sqrt{\tilde{\mu}^2 - (1+2m-2r)^2 \tilde{\Delta}^2}$ and the sum on m depends always on the number of subbands intersected by the chemical potential. At this point we have all the ingredients to define the intraband plasmon analyzing the dispersion and the response function.

We start from the case of electron doping $n = 10^{10}\ \mathrm{cm}^{-2}$ and $R_0 = 500$ Å corresponding to a single occupied subband. We note immediately that $L(q;\omega)$ [see Fig. 6(a)] exhibits two peaks. The first one at lower energy is well defined with shape, spectral weight and position very similar to those we have found for the magnetoplasmon at $\mu = 0$ and $r = 0.5$. On the contrary, the second peak at higher energy is much broader and similar to the peak associated at the interband plasmonlike excitation observed at $\mu = 0$ and $r = 0$. Actually, the effect of the gap closure in the presence of the magnetic field at $\mu = 0$ gives a result very close to what observed for low doping in the absence of the field. Therefore, for low doping (only first subband occupied), we observe that the interband Dirac plasmonlike excitation still survives even if its spectral weight is reduced, but a new well defined excitation (intraband plasmon) gets in.

Finally, to derive the dispersion for long wavelength, we can consider Eq. (22) and replace it in Eq. (19) thus obtaining the behaviors for the case of single occupied subband:

$$\frac{1}{2\pi^2 C_2} \frac{k_F(0)\ \tilde{\mu}\ q^2}{\tilde{\mu}\ \omega^2 - k_F(0)\ q^2} \tilde{V}_q = 1, \qquad (23)$$

which has solution $\omega_p = q\sqrt{C_2^2 k_F^2 \pi + 4 k_F C_2 \tilde{\mu} \tilde{V}_q}/\sqrt{\pi \tilde{\mu}^2}$. We recall that $\tilde{V}_q$ for $q \to 0$ has different trends depending on whether $q \ll 1/R_0$ (one-dimensional) or $q > 1/R_0$ (two-dimensional). For a single subband, we call $k_F(m=0) = k_F$. Therefore we find that the $q \to 0$ behavior for the low-doping

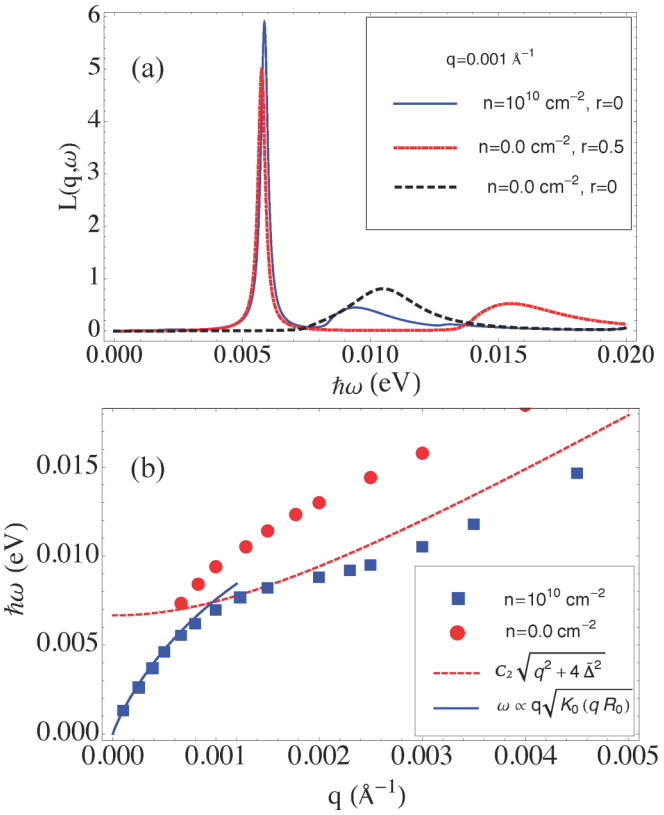

FIG. 6. (a) The dynamic structure factor as a function of the energy (in units of eV) at $R_0 = 500$ Å and $q = 0.001$ Å^{-1} for electronic doping $n = 10^{10}\ \mathrm{cm}^{-2}$ and $r = 0$ (solid blue line), $n = 0$ and $r = 0$ (dashed black line), and $r = 0.5$ (red dotted line). (b) Plasmon dispersion (in units of eV) as a function of the momentum q (in units of Å^{-1}) in the case of single occupied subband with $n = 10^{10}\ \mathrm{cm}^{-2}$ (blue squares) compared with the interband contribution for zero electronic doping (red circles). Interband plasmonlike excitations are present only for energies larger than $C_2\sqrt{q^2 + 4(1-2r)^2\tilde{\Delta}^2(R_0)}$. Note how the analytical solution (continuous line) for small q matches the points obtained numerically.

dispersion is of one-dimensional type with $\omega_p \propto q\sqrt{K_0(q R_0)}$. In Fig. 6(b), the analytic solution of Eq. (23) is shown as the continuous line and shows a very good agreement with the numerical data.

If we apply a magnetic field parallel to the axis of the cylinder, we remove the degeneration of energy subbands. Keeping constant the electron doping to $n = 10^{10}\ \mathrm{cm}^{-2}$ for $R_0 = 500$ Å inevitably the chemical potential changes crossing more subbands. This depends on the ratio r of the fluxes as seen in Eq. (21). Therefore, if we take, for example, a value of $r = 0.4$, the chemical potential crosses two subbands instead of one as before. Even in this case, by exploiting Eq. (22), we can get an analytical solution of the plasmon dispersion for large wavelength. In fact, in the case of two subbands, in the limit of $q \to 0$, the relation in (23) becomes a biquadratic equation because we have a sum on $m = 0$ and $m = -1$ in Eq. (22). Hence, we get four solutions, two for positive frequencies and two with opposite frequencies, as shown in Fig. 7(a) for a specific case. A solution will be of the same type like in the single subband case

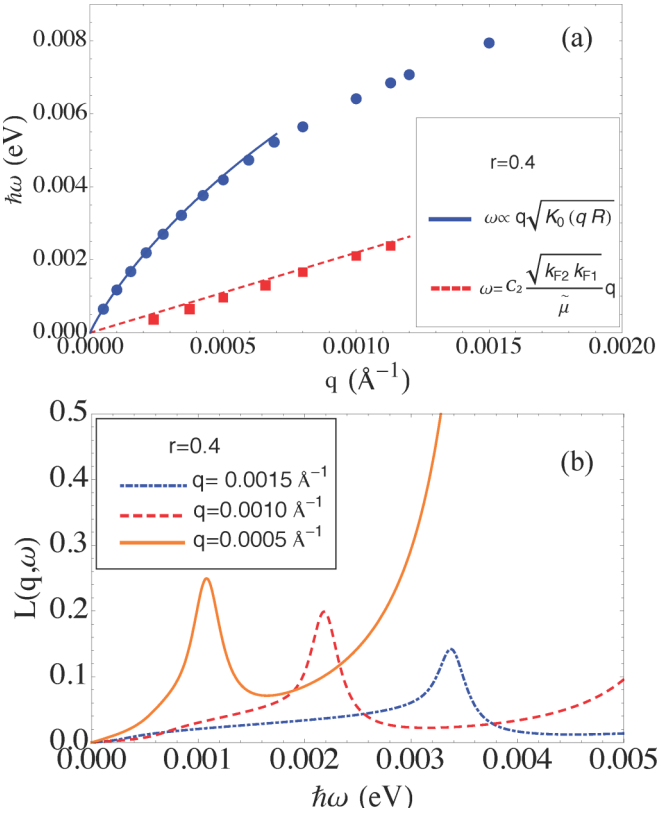

FIG. 7. (a) Plasmon dispersion (in units of eV) as a function of momentum q (in units of Å^{-1}) for $n = 10^{10}$ cm^{-2} and $R_0 = 500$ Å at $r = 0.4$ in the case of two occupied subbands. We distinguish a solution for $\omega > C_2 q$ (blue circles) and an other with a linear behavior for $\omega < C_2 q$ (red squares) where $k_{F1} = k_F(m = 0)$ and $k_{F2} = k_F(m = -1)$. Continuous lines indicate the analytical solutions. (b) The dynamic structure factor as a function of the energy (in units of eV, energy range $\hbar\omega < C_2 q$) for different values of wave vector q at $r = 0.4$ in the case of two occupied subbands with $n = 10^{10}$ cm^{-2}.

$[\omega \sim q\sqrt{K_0(qR_0)}]$, the other will have a linear behavior in q for values $\hbar\omega < C_2 q$. The analytical solution for the linear dispersion provides $\omega = qC_2\sqrt{k_F(0)\, k_F(-1)}/\tilde{\mu}$, although, as shown in Fig. 7(b), this solution has a spectral weight lower than the other for $\hbar\omega > C_2 q$. In fact, for the doping and parameters considered here, the spectral weight of the plasmon peak with linear dispersion is about ten times smaller than the other solution $[\omega \propto q\sqrt{K_0(qR_0)}]$ at higher frequency. For example, if we take a $q = 0.5$ m Å^{-1}, the spectral weights of the two resulting plasmon peaks are 8 meV ($\hbar\omega > C_2 q$) and 0.2 meV ($\hbar\omega < C_2 q$), respectively.

A similar reasoning could be made for any number of subbands in the limit $q \to 0$. However, the analytical solutions of Eq. (19) would become more and more complicated increasing the number of subbands. At fixed radius R_0, increasing the number of subbands means considering higher densities. Also in this case an excitation for $\hbar\omega > C_2 q$ will be observed in the dynamic structure factor and the remaining will be all concentrated in the area $\hbar\omega < C_2 q$ like in the case of two subbands. For example, in a case of higher doping, for example, 5×10^{10} cm^{-2} for $R_0 = 500$ Å, the chemical potential crosses three subbands. We get a plasmon excitation with a behavior of type $\omega_p \propto q\sqrt{K_0(qR_0)}$ and the other two solutions are both linear in q at lower frequencies. The more the electronic doping increases, the more the spectral weight of excitations present at $\hbar\omega < C_2 q$ decreases. In addition, the peak shape observed in the dynamic structure factor for these excitations is no longer a single peak as we see in Fig. 7(b) in the case of two subbands. Indeed, the structure becomes a continuous separated by the higher frequency narrow main peak (present for $\hbar\omega > C_2 q$) whose spectral weight gets enhanced with increasing the electron doping. If the electron doping further increases, the spectral weight of the low frequency continuous becomes negligible in comparison with the main peak.

Up to now, in this section, we have presented all the results for a radius $R_0 = 500$ Å. An increase of the doping requires a larger number M in Eq. (21). When one increases the electron doping up to $n = 10^{12}$ cm^{-2} keeping the radius at $R_0 = 500$ Å, we take into account a number of subbands equal to $M = 20$. If one increases the radius, one reduces the gap and the subbands become more dense. In the case of a larger radius, the effects of the Berry phase are lost since the gap is practically closed and the subbands become a continuous. The two-dimensional limit for the electronic surface states is reached for larger and larger radii. In the case of $R_0 = 4000$ Å^{-1} and high doping about 10^{12} cm^{-2}, we show in Fig. 11 of Appendix A that the plasmon dispersion converges to that of the two-dimensional limit [32].

On the other hand, for a surface doping $n = 10^{12}$ cm^{-2} and at a radius $R_0 = 500$ Å, we actually find significant corrections for the plasmon dispersion compared to the case of an infinite large cylinder (2D Dirac plasmons). Immediately, we observe a difference in the dispersions for large wavelength. In fact, for $q < 1/R_0$, as seen in Fig. 8(a), the dispersion for a radius $R_0 = 500$ Å has one-dimensional features of type $\hbar\omega = \alpha q\sqrt{K_0(qR_0)}$, with $\alpha \sim 33$ eV Å. For small q but such that $q > 1/R_0$, we have the two-dimensional behavior: $\hbar\omega = \beta\sqrt{q}$, with $\beta \sim 1.02$ eV Å$^{1/2}$. A clear dimensional crossover occurs for intraband plasmons in these range of parameters. As discussed in Appendix A, in the case of a radius $R = 4000$ Å for the same doping, one gets a two-dimensional dispersion for all momenta q: $\hbar\omega = \beta_2\sqrt{q}$, with $\beta_2 = \sqrt{(C_2 e^2 k_F^{2D})/2}$ and k_F^{2D} two-dimensional Fermi momentum. Note that, for the chosen parameters, one gets $\beta_2 \sim 0.98$ eV Å$^{1/2}$. Therefore the β coefficient is slightly different from what is found for a Dirac 2D plasmon and depending on the radius.

We notice that the spectral weights for $R_0 = 500$ Å and $R = 4000$ Å are practically identical as it is possible to observe for a particular q in Fig. 8(b). The only tiny difference is seen in the region $0 < \hbar\omega < C_2 q$. In fact, in the case of 2D Dirac plasmon, no structure is observed in that region except for that due to the finite η used for the calculation giving a little imaginary part to the spectrum. For the case of radius $R_0 = 500$ Å instead we see a small structure with a spectral weight that is five orders of magnitude smaller than the weight of the solution for $\hbar\omega > C_2 q$, as shown in the inset of Fig. 8(b). Finally, for values of doping larger than 10^{12} cm^{-2}, the plasmon is very stable and does not undergo significant variations even upon

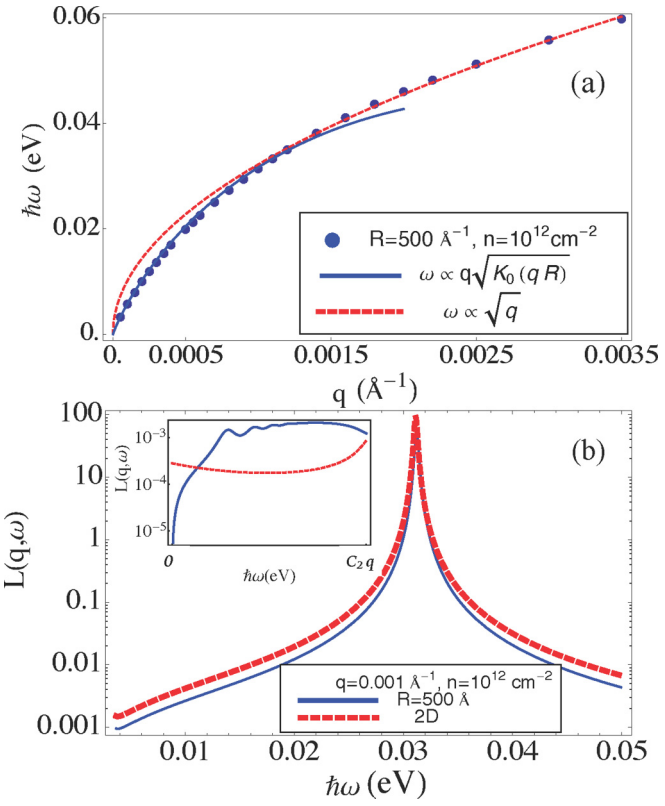

FIG. 8. (a) Plasmon dispersion (in units of eV, circles) as a function of momentum q (in units of Å^{-1}) for $R_0 = 500$ Å and $n = 10^{12}$ cm^{-2}. For $q < 1/R_0$, the dispersion is one-dimensional type: $\hbar\omega = \alpha q\sqrt{K_0(qR_0)}$ (blue solid line) with $\alpha = 33$ eV Å. For $q > 1/R_0$, the dispersion is two-dimensional type: $\hbar\omega = \beta\sqrt{q}$ (red dashed line) with $\beta = 1.02$ eV Å$^{1/2}$. (b) Dynamic structure factor (in logarithmic scale) as a function of the energy (in units of eV) for $q = 0.001$ Å^{-1}, $n = 10^{12}$ cm^{-2}, and $R_0 = 500$ Å. It is compared with the factor of the two-dimensional (2D in figure) infinite surface at the same electron doping and q value. Only in the region $0 < \hbar\omega < C_2 q$, for the cylinder case, there is a continuous structure (in the inset), which is not present for the infinite surface.

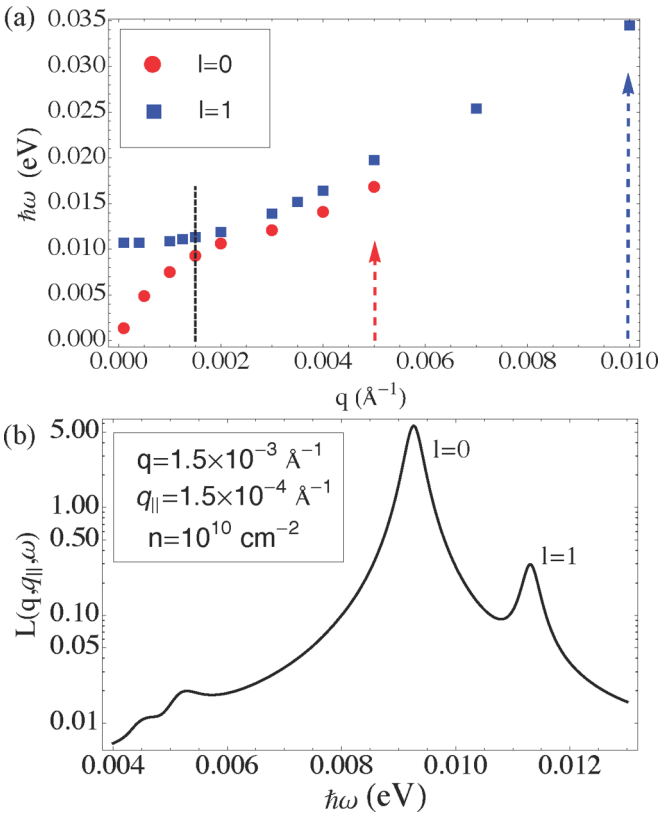

FIG. 9. (a) Energy (in units of eV) of intraband plasmons as a function of wave vector q (in units of Å^{-1}) at $l = 0$ and $l = \pm 1$ for doping $n = 10^{10}$ cm^{-2} and radius $R_0 = 500$ Å. The upper cutoff of q is shown for $l = 0$ (red dashed arrow) and $l = \pm 1$ (blue dashed arrow). (b) Dynamic factor structure as a function of the energy (in units of eV) at $q = 1.5 \times 10^{-3}$ Å^{-1} [black dashed line in (a)] and $q_{||} = 1.5 \times 10^{-4}$ Å^{-1}.

the application of magnetic field. Therefore the Berry phase does not affect the features of the magnetoplasmon in the limit of a large radius or high doping.

Finally, in analogy with the case of zero surface doping, we find the dispersions of intraband plasmonlike excitations at $l \neq 0$ for finite dopings. In Fig. 9, we focus reported only on the value $l = 1$ (which is equal to $l = -1$) for a doping $n = 10^{10}$ cm^{-2} (single occupied subband) and for $R_0 = 500$ Å. Unlike the case of the interband plasmonlike excitations, we see immediately from the Fig. 9(a) that the dispersion for $l > 0$ changes a lot in comparison with that for $l = 0$. In fact, we find for $l = 1$ (analogously to higher l) a plasmon mode whose frequency is higher than that of $l = 0$ and constant for small q. This plasmon dispersion at $l \neq 0$ is typical of cylindrical metallic wires [37]. Even in the case of the intraband plasmon a cutoff exists for the wave vector. However, for intraband plasmons, the plasmon solution is found up to a maximum value of q both for $l = 0$ [red dashed arrow in Fig. 9(a)] and for $l = \pm 1$ [blue dashed arrow in Fig. 9(a)].

We can calculate the spectral weights for all the values of l. To this aim, we focus on values of $q_{||}$ which are an order of magnitude smaller than q. This way, the momentum in nearly parallel to the cylinder axis. Moreover, small values of $q_{||}$ ensures convergence of the series in l by taking a few terms at finite l. For a particular value of $q_{||}$, we have analyzed the contributions for $l > 0$ in comparison with that at $l = 0$. In general, the term at $l = 0$ is always the most important contribution to dynamic structure factor. In Fig. 9(b), by using a logarithmic scale, we show the total dynamic structure factor, which is essentially given by the sum of the contribution of $l = 0$ and $l = \pm 1$. We note immediately that, for a fixed q, the spectral weight associated with $l = 0$ is an order of magnitude larger than the weight related to $l = 1$. So we confirm that for $q_{||} \neq 0$ but small, the relevant contribution is $l = 0$. Another feature that emerges from the Fig. 9(b) is the presence of a small peak at a frequency lower than the peak at $l = 0$. This low-frequency small peak corresponds to a pole that we find from RPA equation always for $l = \pm 1$. This solution presents a minimum and maximum q for which the dispersion exists. Of course, this peak is about two orders of magnitude smaller than the main peak and tends quickly to reduce.

VI. COMPARISON BETWEEN INTER AND INTRABAND PLASMON FEATURES

In this paper, up to now, for intra and interband excitations, we have investigated the dispersion and the damping through the dynamic structure factor. In this section, we clarify the substantial differences that exist between the two modes. By the comparison of the dynamic structure factor in Figs. 3(a) (interband case) and 8(b) (intraband case), we notice that the damping of the interband plasmonlike excitation is much larger than that of intraband modes. In fact, it is possible to observe that the full width at half maximum (FWHM) Γ of the dynamic structure factor at a fixed wave-vector q is larger than that of intra band modes. In order to better analyze the effects of the losses on the mode propagation, we study the behavior of FWHM Γ as a function of q for both zero doping and finite doping ($n = 10^{12}$ cm^{-2}) in correspondence with a radius $R_0 = 500$ Å.

It is possible to observe in Fig. 10(a) that the FWHM Γ associated with the intraband plasmon is zero for values of $q < k_F$, where k_F is indicated by a blue dashed line. In fact, the FWHM Γ appears to be of the same order of the parameter η indicated as a black dashed line in Fig. 10(a) (η is equal to 1.5×10^{-4} eV in this paper). We have checked that, if we send η to zero, then also Γ of intraband plasmons goes to zero for $q < k_F$. On the other hand, again for intraband plasmons, we notice a rapid increase of Γ for $q > k_F$. This behavior of the intraband FWHM is very similar to that observed in the case of a two-dimensional system [32]. Therefore, in the case of infinite radius, we recover not only the plasmon dispersion plasmon but also the behavior of the damping associated with it.

A different situation occurs for interband plasmonlike excitations. As shown in Fig. 10(a), Γ for interband plasmons is different from zero for small values of the wave vector q. Indeed, the value of Γ is at least one order of magnitude larger than η. Considering the peak values of interband plasmons shown in Fig 3(a), we point out that, for $q = 0.001$ Å, Γ is about 3×10^{-3} eV, while the peak energy is around 10^{-2} eV. Therefore, for $q = 0.001$ Å, Γ is about one third of the peak energy indicating that the interband plasmon is severely damped. We remark that intraband plasmons have a zero Γ for the same values of wave vectors. Moreover, again in contrast with the intraband case, Γ for interband plasmons goes to zero with increasing q. We stress that the decrease of Γ with increasing q does not mean that the interband plasmon is more defined. In fact, we have checked that the spectral weight related to the peaks of the dynamic structure factor rapidly decreases with increasing q. Actually, for $q = 0.05$ Å, the spectral weight can be assumed as virtually zero. This behavior is again different when compared to the intraband case.

In the inset of Fig. 10(b), we report the plasmon group velocity $\partial\omega/\partial q$ (in units of 10^7 cm s^{-1}) derived from plasmon dispersions. Interband and intraband plasmon modes show different behaviors as a function of q. In fact, the intraband velocity is monotonically decreasing, while the interband plasmon is quite constant with increasing q. Actually, interband velocity slowly increases reaching a plateau that converges to the asymptotic value equivalent to $C_2/\hbar$. In fact, at zero doping, for enough large q, the plasmon dispersion flattens on

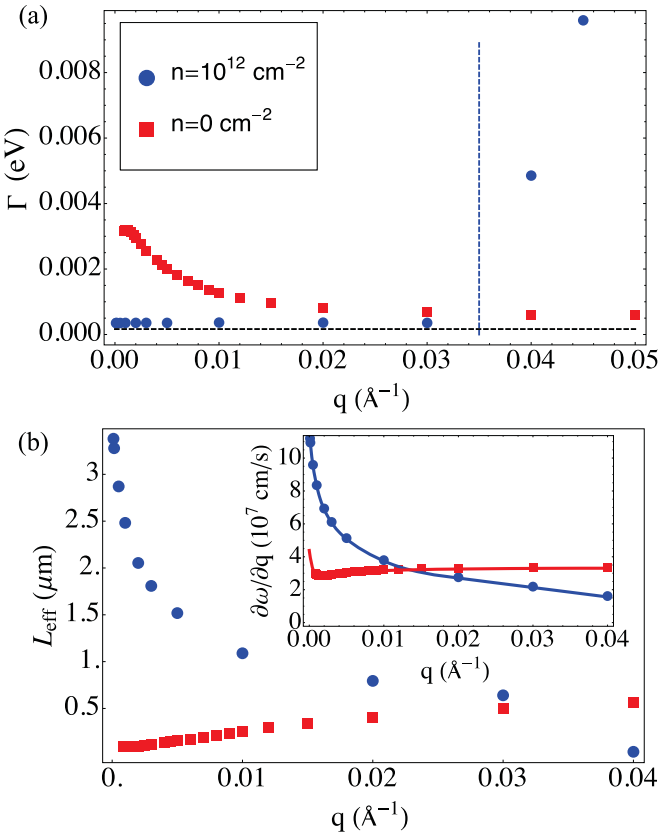

FIG. 10. (a) Full width at half maximum Γ (in units of eV) as a function of q (in units of Å^{-1}) for inter (zero surface doping, red squares) and intraband (surface doping $n = 10^{12}$ cm^{-2}, blue circles) plasmons in correspondence with a radius $R_0 = 500$ Å. The surface doping $n = 10^{12}$ cm^{-2} corresponds to a Fermi wave-vector $k_F = 0.035$ Å^{-1} (dashed blue line). Note as the damping of intraband plasmon is close to η (dashed black line) for $q < k_F$. (b) Propagation distance (in units of micrometers) for inter (zero surface doping, red squares) and intraband (surface doping $n = 10^{12}$ cm^{-2}, blue circles) plasmons as a function of q (in units of Å^{-1}) in correspondence with a radius $R_0 = 500$ Å. In the inset, the velocity (in units of 10^7 cm s^{-1}) as a function of q (in units of Å^{-1}) for inter (zero surface doping, red squares) and intraband (surface doping $n = 10^{12}$ cm^{-2}, blue circles) plasmons.

a value equal to $C_2 q$. We conclude from the features of the velocity that the nature of the interband plasmon is profoundly different from the intraband one.

Finally, it is also possible to calculate the plasmon propagation length L_{eff}, which is so defined: $L_{\text{eff}} = \Gamma^{-1}\partial\hbar\omega/\partial q$. Of course, in addition to the average life time ($\hbar\Gamma^{-1}$), this distance is also related to the group velocity of the plasmon modes. In Fig. 10(b), we show the propagation length associated with different values of q in the case of interband and intraband plasmons. It is possible to observe how the intraband plasmon, in the range where it has a value of Γ close to zero, has a length greater than the interband one. For example, for $q = 0.001$ Å, L_{eff} is of the order of 3 μm for intraband plasmon, while it is of the order of 0.2 μm for the interband plasmon. Therefore intraband plasmons show lengths slightly smaller than those in metals, whose surface plasmons propagate on

distances of the order of ten micrometers [37]. On the other hand, interband plasmons are characterized by small axial propagation lengths comparable with the radius of the cylinder. The intraband and interband lengths have opposite behaviors as a function of the wave vector q. With increasing q, the intraband length decreases very fast, while the interband length slowly increases. In the intraband case, only for $q > k_F$, the lengths become comparable with the interband ones.

VII. CONCLUSIONS

In this paper, we have studied the charge response of a cylindrical wire of the TI Bi_2Se_3. We have provided an analytical solution of the dynamic structure factor within the RPA approximation for the electron-electron Coulomb interaction. We have analyzed how the Berry phase and the interference on it due to an axial magnetic field affect the plasmon dispersion and spectral weights of a TI cylinder.

One of the main results of the work is that, in the case of zero surface doping ($\mu = 0$), interband plasmonlike excitations can form in TI nanowires unlike in TI slabs. In particular, a strong dependence of this class of excitations on an axial magnetic field has been observed due to the interference effects between the Berry phase and magnetic field. Actually, an axial magnetic field induces a change in dispersion and peak shape of the magnetoplasmon, which becomes more defined with a longer lifetime.

Then, we have considered the case of a low surface electron doping of about 10^{10} cm^{-2} when the chemical potential crosses one subband in the absence of magnetic field. We have stressed that the resulting plasmon excitation has both dispersion and spectral weight similar to those of a magnetoplasmon at zero surface doping. In this case, it is has been also possible to calculate the limit for $q \to 0$ of the polarization function analytically solving the RPA equation and providing the dispersion of intraband plasmons. The application of a magnetic field removes the degeneration of subbands giving rise to two types of excitations: one for $\omega > C_2 q$ with a behavior $\omega \propto q\sqrt{\tilde{V}_q}$, and another for $\omega < C_2 q$ with a linear behavior as a function of q. The most important difference between these two kinds of solution is in the spectral weight which is much larger for plasmons at $\omega > C_2 q$.

Finally, we have checked that the limit of infinite two-dimensional surface is reached for a very large radius, for example, $R_0 = 4000$ Å at a large surface doping of 10^{12} cm^{-2}. We have also analyzed corrective terms to the case of the two-dimensional limit in the plasmon dispersion. To this aim, we have considered the same surface doping of 10^{12} cm^{-2} but with a smaller radius equal to $R_0 = 500$ Å. In any case, for high doping, we have pointed out that the effects induced by an axial magnetic field are no more important. We point out that quite large changes of doping have been already achieved with a gate geometry in TI [40], in particular in thin films [41]. Therefore we believe that it is not impossible to tune experimentally the doping in TI nanowires from small to large values.

The focus of this paper has been on the case when, in the dynamic structure factor, the momentum $\mathbf{q}_{||}$ parallel to $x - y$ plane (orthogonal to the axis z of the cylinder) is zero. We have also studied the effects of $\mathbf{q}_{||} \neq 0$ analyzing charge excitations where the angular degrees of freedom are more involved. It could be interesting to consider not only the presence of Dirac surface plasmons but also of other plasmon excitations [42], in particular of surface plasmons [43] related to bulk charge carriers which have been observed very recently in EELS experiments [44,45]. Finally, it could be useful to study plasmon features at finite temperatures analyzing the effects of electron-phonon couplings [46–48], in particular, in the case of wires freely suspended or grown on a substrate [49]. Work in this direction is in progress.

ACKNOWLEDGMENTS

C.A.P. acknowledges partial financial support from the CNR-INFN national project (PREMIALE 2012) EOS Organic Electronics for Innovative Research Instrumentation. C.A.P. and V.C. acknowledge partial financial support from the Campania region project L.R. 5/2002 year 2007 Role of interfaces in magnetic strongly correlated oxides: manganite heterostructures.

APPENDIX A: CALCULATION AND LARGE RADIUS LIMIT OF THE POLARIZATION FUNCTION AND PLASMON DISPERSION

As discussed in Sec. II, we consider the surface wave functions of a TI cylindrical wire obtained from previous works [10,11]:

$$\psi^s_{k,m}(\rho,\phi,z) = \sqrt{\frac{1}{4\pi L}} e^{ikz} R(\rho) e^{im\phi} \mathbf{u}^s_{k,m}(\phi), \tag{A1}$$

where L is the length along the z axis, $R(\rho)$ is the radial function, $\mathbf{u}^s_{k,m}(\phi)$ is a quadrispinor depending on the angular variable ϕ. In Eq. (A1), the radial function $R(\rho)$ is zero for $\rho \geqslant R_0$, while, for $0 < \rho < R_0$, it is the following:

$$R(\rho) = N e^{-\alpha_- R_0}(e^{(\alpha_+ + \alpha_-)\rho} - e^{\alpha_+ R_0 + \alpha_- \rho}), \tag{A2}$$

with N normalization constant,

$$\alpha_\pm = \frac{1 \pm \sqrt{1+4a}}{2L_0},$$
$$a = -\frac{M_2 M_0}{A^2}, \quad L_0 = \frac{M_2}{A}.$$

In Eq. (A1), for negative eigenvalues $\epsilon^-_{k,m}$, the quadrispinor is

$$\mathbf{u}^-_{k,m}(\phi) = \begin{bmatrix} \frac{1}{2} + \alpha_{k,m} + i\beta_{k,m} \\ -\frac{i}{2} + i(\alpha_{k,m} + i\beta_{k,m}) \\ -\frac{e^{i\phi}}{2} + e^{i\phi}(\alpha_{k,m} + i\beta_{k,m}) \\ \frac{1}{2} i e^{i\phi} + i e^{i\phi}(\alpha_{k,m} + i\beta_{k,m}) \end{bmatrix}, \tag{A3}$$

while, for positive eigenvalues $\epsilon^+_{k,m}$, it is

$$\mathbf{u}^+_{k,m}(\phi) = \begin{bmatrix} \frac{1}{2} - (\alpha_{k,m} + i\beta_{k,m}) \\ -\frac{i}{2} - i(\alpha_{k,m} + i\beta_{k,m}) \\ -\frac{e^{i\phi}}{2} - e^{i\phi}(\alpha_{k,m} + i\beta_{k,m}) \\ \frac{1}{2} i e^{i\phi} - i e^{i\phi}(\alpha_{k,m} + i\beta_{k,m}) \end{bmatrix} \tag{A4}$$

with

$$\alpha_{k,m} = \frac{\left(\frac{1}{2}+m-r\right)C_1}{2\sqrt{C_2^2\mathrm{k}^2+\left(\frac{1}{2}+m-r\right)^2 C_1^2}}, \tag{A5}$$

$$\beta_{k,m} = \frac{C_2 k}{2\sqrt{C_2^2\mathrm{k}^2+\left(\frac{1}{2}+m-r\right)^2 C_1^2}}. \tag{A6}$$

We can evaluate the term $\chi_0(z-z',\phi-\phi';\omega)$ present in Eq. (6) for the full susceptibility:

$$\chi_0(z-z',\phi-\phi';\omega) = \frac{1}{(2\pi L)^2}\sum_{k,q,m,l,s,s'} e^{iq(z-z')}e^{il(\phi-\phi')}\frac{f\left(\epsilon^s_{k,m}\right)-f\left(\epsilon^{s'}_{k+q,m+l}\right)}{\epsilon^s_{k,m}-\epsilon^{s'}_{k+q,m+l}+\hbar(\omega+i0^+)}F^{s,s'}(k,q,m,l), \tag{A7}$$

where q is the momentum along z axis, l is the angular number, and $F^{s,s'}(k,q,m,m+l)$ is the scalar product between the eigenvectors in (A3) and (A4):

$$F^{s,s'}(k,q,m,m+l) = \frac{1}{2}\left[1+ss'\frac{\tilde{\Delta}^2(R_0)(1+2m+2l)(1+2m)+k(k+q)}{\sqrt{\tilde{\Delta}^2(R_0)(1+2m)+k^2}\sqrt{\tilde{\Delta}^2(R_0)(1+2m+2l)+(k+q)^2}}\right], \tag{A8}$$

with

$$\tilde{\Delta}(R_0) = \frac{C_1}{2C_2R_0}.$$

Finally, transforming in Eq. (A7) the discrete sum over k in a integral, we get the polarization function $\chi_0(q,l;\omega)$ used in the main text:

$$\chi_0(q,l;\omega) = \frac{1}{(2\pi)^2}\int dk \sum_{m,s,s'} \times \frac{f\left(\epsilon^s_{k,m}\right)-f\left(\epsilon^{s'}_{k+q,m+l}\right)}{\epsilon^s_{k,m}-\epsilon^{s'}_{k+q,m+l}+\hbar(\omega+i0^+)}F^{s,s'}(k,q,m,l). \tag{A9}$$

The polarization function in Eq. (A9) is expressed in terms of a sum on m. We will show that, in the limit of infinite radius, the double sum in k and m will transform in a bi-dimensional integral over $\mathbf{k}$. Therefore Eq. (A9) becomes the susceptibility of a 2D problem in the large radius limit. To this aim, for simplicity, we take only the contributions for $l=0$. The energy for our problem is defined as $\epsilon_{k,m} = \pm C_2\sqrt{k^2+(m+1/2)^2/R_0^2}$ having considered $C_1 = C_2$. In the 2D case, we have $\epsilon_k = \pm\hbar v_F\sqrt{k^2+k_{||}^2}$, where $C_2 = \hbar v_F$, k is the same associated to z direction and $\mathbf{k}_{||}$ is the other momentum in the plane. If we set $R_0\to\infty$, also the parameter $m\to\infty$, and, if $k_{||} = \frac{2\pi}{L}m$, where $L = 2\pi R_0$, then in this limit $m/R_0 \to k_{||}$. The factor $1/2$ due to Berry phase, in the limit of large radius, is no longer relevant. Automatically, even the prefactors $F^{s,s'}(k,q,m,m+l)$ become the two-dimensional ones:

$$F^{s,s'}(k,|\mathbf{k}_{||}|,q) = \frac{1}{2}\left[1+ss'\frac{k(k+q)+k_{||}^2}{\sqrt{k^2+k_{||}^2}\sqrt{(k+q)^2+k_{||}^2}}\right]. \tag{A10}$$

Finally, the discrete sum on m becomes a continuum such that $\sum_m \to R_0\int dk_{||}$. Naturally, we note that between $\chi_0(q;\omega)$ and $\chi_{2D}(q;\omega)$ there is a length factor of difference, therefore, we conclude that

$$\frac{1}{R_0}\chi_0(q;\omega) \xrightarrow{R_0\to\infty} \chi_{2D}(q;\omega), \tag{A11}$$

where $\chi_{2D}(q;\omega)$ is

$$\chi_{2D}(q,\omega) = \frac{1}{(2\pi)^2}\int d\mathbf{k}\sum_{s,s'}\frac{f\left(\epsilon^s_k\right)-f\left(\epsilon^{s'}_{k+q}\right)}{\epsilon^s_k-\epsilon^{s'}_{k+q}+\hbar(\omega+i0^+)} \times F^{s,s'}(k,k_{||},q). \tag{A12}$$

If we also considered contributions for $l\neq 0$, in addition to the momentum q another transferred momentum $q_{||}$ of transversal type to the axis of the cylinder would appear.

We can find through the electron density function, the equation of the RPA theory given by $1-\tilde{V}_{q,l}\chi_0(q,l;\omega)=0$, which provides the condition for plasmon formation in the system. For this reason, we need to expand the Coulomb potential in the cylindrical coordinates as follows:

$$V(\vec{r}-\vec{r'}) = \frac{2}{\pi}\sum_{m=-\infty}^{\infty}\int_0^\infty dk I_m(kr_<)K_m(kr_>) \times e^{im(\phi-\phi')}\cos[k(z-z')], \tag{A13}$$

which, by using translational invariance in the z direction, becomes

$$V(q;\mathbf{r},\mathbf{r}') = 2\sum_{m=-\infty}^{\infty} I_m(|q|r_<)K_m(|q|r_>)e^{im(\phi-\phi')}, \tag{A14}$$

where we used

$$\int dz e^{-iq(z-z')}\cos[k(z-z')] = 2\pi\frac{1}{2}[\delta(q-k)+\delta(q+k)]. \tag{A15}$$

From the definition, the induced density can be written as $d(\vec{r}) = \int d\vec{r'}d\vec{r''}\chi(\vec{r},\vec{r'})V(\vec{r'}-\vec{r''})d(\vec{r''})$ where $\chi(\vec{r},\vec{r'};\omega) = R(\rho)^2R(\rho')^2\chi_0(z-z',\phi-\phi';\omega)$ is the susceptibility. Passing

in Fourier transform in q and in l, and replacing Eqs. (A7) and (A14) in $d(\vec{r})$, we have that the density is given by

$$d_{q,l}(r) = 4\pi e^2 \chi_0(q,l) \int d\rho' \rho' R(\rho)^2 R(\rho')^2 \times \int d\rho'' \rho'' I_n(|q|\rho_<) K_n(|q|\rho_>) \cdot d_{q,l}(\rho''). \quad \text{(A16)}$$

If we define

$$S_{q,l}(\rho'') = \int d\rho' \rho' R(\rho')^2 I_l(|q|\rho_<) K_l(|q|\rho_>) = K_l(|q|\rho'') \int_0^{\rho''} d\rho' \rho' R(\rho')^2 I_l(|q|\rho') + I_l(|q|\rho'') \int_{\rho''}^{R_0} d\rho' \rho' R(\rho')^2 K_l(|q|\rho'), \quad \text{(A17)}$$

and multiplying by $S_{q,l}(\rho)$ to the left and right member and integrating over ρ, Eq. (A16) becomes

$$1 = \chi_0(q,l) \tilde{V}_{q,l}, \quad \text{(A18)}$$

where we called $\tilde{V}_{q,l} = 4\pi e^2 \int d\rho\rho R(\rho)^2 S_{q,l}(\rho)$.

Recalling that $l = 0$, we note that, if R_0 is very large, for long wavelength $qR_0 \ll 1$, thus we can write

$$R_0 \tilde{V}_{q,l=0} = 4\pi e^2 R_0 \int d\rho\rho R(\rho)^2 S_{q,0}(\rho) \mapsto 4\pi e^2 R_0 \, I_0(qR_0) K_0(qR_0) \mapsto \frac{2\pi e^2}{q}, \quad \text{(A19)}$$

which is the transformed of the two-dimensional Coulomb potential. Therefore Eq. (A18) for large R_0 becomes

$$1 = \frac{1}{R_0} \chi_0(q,0) \frac{2\pi e^2}{q},$$

where, in this limit, from Eq. (A11), $\chi_0(q,0)/R_0$ converges towards the two-dimensional susceptibility. As shown in Fig. 11, the plasmon dispersion of the infinite radius nanowire converges to that of a 2D problem ($\omega \propto \sqrt{q}$).

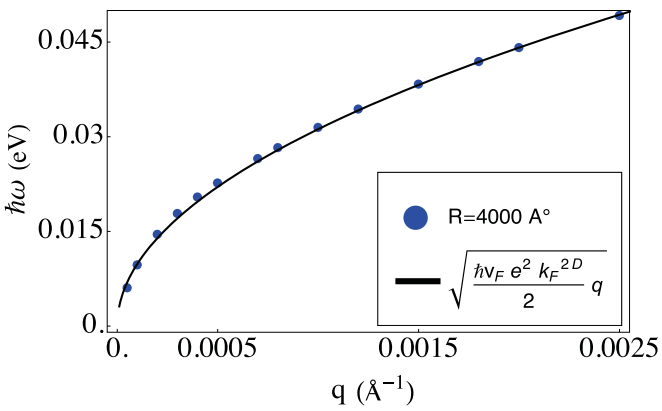

FIG. 11. The plasmon dispersion as a function of the momentum q along z for a cylindrical wire of radius $R = 4000$ Å. The result is compared with that of an infinite plane (translational invariance along all two directions [32]). In this limiting case, there is an analytical form for the plasmon dispersion, which is reported in the figure.

As discussed in Sec. III, we can derive the induced density and potential in correspondence with the plasmon frequencies. Upon substituting Eq. (A18) in Eq. (A16), one immediately finds that, in our approach, the induced density corresponding to a mode with given q and l is the following:

$$d(\rho,z,\phi) = B_{q,l}(R_0) R^2(\rho) e^{iqz} e^{il\phi}, \quad \text{(A20)}$$

where $B_{q,l}(R_0)$ is an arbitrary constant dependent not only on q and l, but also on the cylinder radius R_0. As expected, the density depends on the radial function $R^2(\rho)$, which, for a sufficiently large radius, is peaked practically only on the lateral surface of the cylinder.

From the density, one can determine the electrical potential Φ corresponding to a plasmon with given q and l:

$$\Phi(\rho,z,\phi) = e^{iqz} e^{il\phi} B_{q,l}(R_0) \times \int_0^{R_0} d\rho' \rho' R^2(\rho') K_l(q\rho_>) I_l(q\rho_<). \quad \text{(A21)}$$

Equation (A21) can be specialized to the case $\rho < R_0$, yielding Φ^{int} (potential internal to the cylinder)

$$\Phi^{\text{int}}(\rho,z,\phi) = e^{iqz} e^{il\phi} B_{q,l}(R_0) \times \left[K_l(q\rho) \int_0^{\rho} d\rho' \rho' R^2(\rho') I_l(q\rho') - I_l(q\rho) \int_{\rho}^{R_0} d\rho' \rho' R^2(\rho') K_l(q\rho') \right], \quad \text{(A22)}$$

and to case $\rho > R_0$, providing Φ^{ext} (potential external to the cylinder),

$$\Phi^{\text{ext}}(\rho,z,\phi) = e^{iqz} e^{il\phi} B_{q,l}(R_0) \times K_l(q\rho) \int_0^{R_0} d\rho' \rho' R^2(\rho') I_l(q\rho'). \quad \text{(A23)}$$

Recalling that the associated electric field is given by $\vec{E}(\vec{r}) = -\nabla\Phi(\vec{r})$, we can derive the cylindrical components (E_ρ, E_z, E_ϕ) of the field in correspondence with a plasmon mode. We stress that for $l = 0$ the contribution $E_\phi = 0$ in all the space, so that, for this mode, only the longitudinal and radial components of the field survive. Therefore the $l = 0$ mode bears strong similarity with the TM mode found in correspondence with surface plasmons of metallic cylinders only for $l = 0$ [37]. In our case, we have analyzed the electrostatic limit, therefore the axial component of the magnetic field is clearly zero.

We observe that for the radii analyzed in this paper ($R_0 \geqslant 500$ Å), the radial wave function present in Eqs. (A22) and (A23) can be approximated as a delta function: $R^2(\rho) \simeq \delta(\rho - R_0)/R_0$. Clearly, this approximation becomes better and better with increasing the radius of the cylinder. Therefore the induced density ρ becomes different from zero only on the lateral surface whose charge density is proportional to $1/R_0$. We can provide analytical expressions for the electric field

focusing in particular on the modes with $l = 0$:

$$(E_\rho, E_z) = B_{q,l=0}(R_0)\begin{cases}(q\,I_1(q\rho)K_0(q\,R_0)e^{iqz},\ iq\,I_0(q\rho)K_0(q\,R_0)e^{iqz}), & \rho \leqslant R_0,\\ (-q\,K_1(q\rho)I_0(q\,R_0)e^{iqz}, iq\,K_0(q\rho)I_0(q\,R_0)e^{iqz}), & \rho > R_0.\end{cases} \tag{A24}$$

We point out that the longitudinal component E_z is continuous at $\rho = R_0$, while the radial component E_ρ is discontinuous. Actually, using the Wronskian of the modified Bessel functions of zero order [37], one can prove that the difference $E_\rho(\rho \to R_0^+) - E_\rho(\rho \to R_0^-)$ is proportional to $1/R_0$, hence, proportional to the charge surface density relative to the lateral surface of the cylinder. Inside the cylinder ($\rho < R_0$), the radial component E_ρ goes as $I_1(q\rho)$, therefore, at finite q, E_ρ is proportional to $q\rho$ for very small values of ρ. On the other hand, outside the cylinder ($\rho > R_0$), E_ρ goes as $K_1(q\rho)$, therefore, at finite q, E_ρ is proportional to $e^{-q\rho}/\sqrt{q\rho}$ for very large values of ρ.

It is interesting to determine the behavior of the electric field in different limits. For large wavelengths (small q, with $q \ll 1/R_0$), the field in Eq. (A24) becomes

$$\begin{aligned} E_\rho &\propto \frac{q^2\rho}{2}K_0(q\,R_0), \quad \rho \leqslant R_0,\\ E_\rho &\propto -\frac{1}{\rho}I_0(q\,R_0), \quad \rho > R_0,\\ E_z &\propto iq\left(1+\frac{q^2\rho^2}{4}\right)K_0(q\,R_0), \quad \rho \leqslant R_0,\\ E_z &\propto -iq\log(q\rho)I_0(q\,R_0), \quad R_0 < \rho < 1/q, \end{aligned} \tag{A25}$$

recalling that the modified Bessel functions can be written as $I_0(q\rho) \sim (1 + q^2\rho^2/4)$ and $K_0(q\rho) \sim -\log(q\rho)$ for $q\rho \ll 1$. In particular, from Eq. (A25) emerges that, for $q \to 0$, as expected, the electric field inside the cylinder ($\rho < R_0$) is zero. In the same limit $q \to 0$, outside the cylinder ($\rho > R_0$), the longitudinal component E_z vanishes, while the radial component E_ρ goes as $1/\rho$. We can also determine the electric field in the limit of small wavelengths (large q, with $q > 1/R_0$):

$$\begin{aligned} E_\rho &\propto \frac{1}{\sqrt{2\pi q}}e^{q\rho}\frac{(2q\rho-1)}{2\rho^{3/2}}K_0(q\,R_0), \quad \rho \leqslant R_0,\\ E_\rho &\propto -\sqrt{\frac{\pi}{2q}}e^{-q\rho}\frac{(2q\rho+1)}{2\rho^{3/2}}I_0(q\,R_0), \quad \rho > R_0,\\ E_z &\propto iq\frac{1}{\sqrt{2\pi q\rho}}e^{q\rho}K_0(q\,R_0), \quad \rho \leqslant R_0,\\ E_z &\propto iq\frac{\sqrt{\pi}}{\sqrt{2q\rho}}e^{-q\rho}I_0(q\,R_0), \quad \rho > R_0, \end{aligned} \tag{A26}$$

recalling that the Bessel functions can be written as $I_0(q\rho) \sim e^{q\rho}/\sqrt{2\pi q\rho}$ and $K_0(q\rho) \sim e^{-q\rho}\sqrt{\pi/2q\rho}$ for $q\rho > 1$.

APPENDIX B: CALCULATION OF THE INVERSE DIELECTRIC FUNCTION AND DYNAMIC STRUCTURE FACTOR

In this appendix, we calculate the inverse of the dielectric constant and, then, the dynamic structure factor. This calculation could be extended to any type of geometry, although here for simplicity it is specialized for a cylindrical case. Exploiting the symmetries of the cylinder and using Eq. (A13), the dielectric constant given in Eq. (7) can be written as

$$\epsilon(\vec{r},\vec{r'}) = \frac{\delta(\rho-\rho')}{\rho}\delta(\phi-\phi')\delta(z-z') - \frac{2}{L}R(\rho')^2\sum_{q_z}e^{iq_z(z-z')}\sum_l e^{il(\phi-\phi')}S_{q_z,l}(\rho)\chi_0(q_z,l). \tag{B1}$$

The inverse dielectric function is so defined

$$\int d\vec{r}_1\epsilon^{-1}(\vec{r},\vec{r}_1)\epsilon(\vec{r}_1,\vec{r'}) = \delta(\vec{r}-\vec{r'}). \tag{B2}$$

Using q and l and replacing Eq. (B1) in Eq. (B2), we get

$$\int d\rho_1\rho_1\epsilon^{-1}_{q,l}(\rho,\rho_1) \times\left(\frac{\delta(\rho_1-\rho')}{\rho_1} - 4\pi\,R(\rho')^2S_{q,l}(\rho_1)\chi_0(q,l)\right) = \frac{\delta(\rho-\rho')}{\rho}. \tag{B3}$$

We need to solve an integral equation with a separable variable kernel. If we define $A_{q,l}(\rho) = \int d\rho_1\rho_1\epsilon^{-1}_{q,l}(\rho,\rho_1)S_{q,l}(\rho_1)$ and we multiply for $S_{q,l}(\rho')$, integrating both members over ρ', the integral equation becomes

$$A_{q,l}(\rho)\left[1 - 4\pi\,\chi_0(q,l)\int d\rho'\rho'R(\rho')^2S_{q,l}(\rho')\right] = S_{q,l}(\rho). \tag{B4}$$

We note that the equation in square parenthesis is equal to Eq. (A18) since $\tilde{V}_{q,l} = 4\pi\int d\rho'\rho'R(\rho')^2S_{q,l}(\rho')$. This way, it is possible find the term $A_{q,l}$ from Eq. (B4) that replaced in (B3) returns

$$\epsilon^{-1}_{q,l}(\rho,\rho') = \frac{\delta(\rho-\rho')}{\rho} + \frac{S_{q,l}(\rho)\chi_0(q,l)R(\rho')^2}{1-\chi_0(q,l)_{q,l}}. \tag{B5}$$

Finally, we can write a dynamic structure factor in this form:

$$L(\omega,q,q_{||}) = -\mathrm{Im}\left[\frac{1}{V}\iint d\vec{r}d\vec{r'}\epsilon^{-1}(\vec{r},\vec{r'})e^{-i\vec{q}\cdot\vec{r}}e^{i\vec{q}\cdot\vec{r'}}\right], \tag{B6}$$

where V is the volume enclosed by the cylinder. Exploiting the cylindrical symmetries and passing in Fourier transform with $\epsilon^{-1}(\vec{r},\vec{r'}) = \frac{1}{L}\sum_q e^{iq(z-z')}\frac{1}{2\pi}\sum_l e^{il(\phi-\phi')}\epsilon^{-1}_{q,l}(\rho,\rho')$, we get for the only integral part over z and z' in (B6):

$$\frac{1}{L^2}\frac{L}{2\pi}\int dq\iint dzdz'e^{i(q-q)z}e^{i(q-q)z'} = 1. \tag{B7}$$

Finally, we have

$$L(\omega,q,q_{||}) = -\frac{1}{2\pi^2 R_0^2}\mathrm{Im}\left[\sum_l \frac{\chi_0(q_z,l;\omega)}{1-\chi_0(q,l;\omega)\tilde{V}_{q,l}} \int d\rho' \rho' d\phi' e^{i|q_{||}|\rho'\cos\phi'} e^{-il\phi'} R(\rho')^2 \int d\rho\rho d\phi e^{i|q_{||}|\rho\cos\phi} e^{il\phi} S_{q,l}(\rho)\right], \quad \text{(B8)}$$

where both the integrals in ϕ and ϕ' return the Bessel functions $4\pi^2 \mathrm{J}_l(|q_{||}|\rho)\mathrm{J}_l(|q_{||}|\rho')$. The integral in (B8) is thus obtained:

$$L(q,q_{||};\omega) = -\frac{2}{R_0^2}\mathrm{Im}\left[\sum_l \frac{\chi_0(q,l;\omega)}{1-\chi_0(q,l;\omega)\tilde{V}_{q,l}} \int_0^{R_0} d\rho' \rho' \,\mathrm{J}_l(|q_{||}|\rho') R(\rho')^2 \int_0^{\infty} d\rho\rho \,\mathrm{J}_l(|q_{||}|\rho) S_{q,l}(\rho)\right]. \quad \text{(B9)}$$

We notice that the second integral in Eq. (B9) depends on $S_{q,l}$, which is linked to the Coulomb potential. Since the Coulomb interaction between electrons is effective in the whole space, inside and outside the material, the integration limits of the radial variables are extended from zero to infinity.

[1] S.-Q. Shen, *Topological Insulators - Dirac Equation in Condensed Matters* (Springer, Berlin, Heidelberg, 2012).

[2] B. A. Bernevig, *Topological Insulators and Topological Superconductors* (Princeton University Press, Princeton, New Jersey, 2013).

[3] D. Hsieh, Y. Xia, D. Qian, L. Wray, J. H. Dil, F. Meier, L. Patthey, J. Osterwalder, A. V. Fedorov, H. Lin, A. Bansil, D. Grauer, Y. S. Hor, R. J. Cava, and M. Z. Hasan, Nature (London) **460**, 1101 (2009).

[4] P. Roushan, J. Seo, C. V. Parker, Y. S. Hor, D. Hsieh, D. Qian, A. Richardella, M. Z. Hasan, R. J. Cava, and A. Yazdani, Nature (London) **460**, 1106 (2009).

[5] D. Hsieh, Y. Xia, L. Wray, D. Qian, A. Pal, J. H. Dil, J. Osterwalder, F. Meier, G. Bihlmayer, C. L. Kane, Y. S. Hor, R. J. Cava, and M. Z. Hasan, Science **323**, 919 (2009).

[6] H. Zhang, C.-X. Liu, X.-L. Qi, Xi Dai, Z. Fang, and S.-C. Zhang, Nat. Phys. **5**, 438 (2009).

[7] H. Peng, K. Lai, D. Kong, S. Meister, Y. Chen, X.-L. Qi, S.-C. Zhang, Z.-X. Shen, and Y. Cui, Nat. Mater. **9**, 225 (2010).

[8] S. S. Hong, Y. Zhang, J. J. Cha, X.-L. Qi, and Yi Cui, Nano Lett. **14**, 2815 (2014).

[9] J. Dufouleur, L. Veyrat, A. Teichgräber, S. Neuhaus, C. Nowka, S. Hampel, J. Cayssol, J. Schumann, B. Eichler, O. G. Schmidt, B. Büchner, and R. Giraud, Phys. Rev. Lett. **110**, 186806 (2013).

[10] K.-I. Imura, Y. Takane, and A. Tanaka, Phys. Rev. B **84**, 195406 (2011).

[11] P. Iorio, C. A. Perroni, and V. Cataudella, Eur. Phys. J. B **89**, 97 (2016).

[12] H. Zhang, X. Zhang, C. Liu, S.-T. Lee, and J. Jie, ACS Nano **10**, 5113 (2016).

[13] D. Pesin and A. H. MacDonald, Nat. Mater. **11**, 409 (2012).

[14] P. Di Pietro, M. Ortolani, O. Limaj, A. Di Gaspare, V. Giliberti, F. Giorgianni, M. Brahlek, N. Bansal, N. Koirala, S. Oh, P. Calvani, and S. Lupi, Nat. Nanotechnol. **8**, 556 (2013).

[15] M. Autore, H. Engelkamp, F. D'Apuzzo, A. Di Gaspare, P. Di Pietro, I. Lo Vecchio, M. Brahlek, N. Koirala, S. Oh, and S. Lupi, ACS Photon. **2**, 1231 (2015).

[16] M. Autore, F. Giorgianni, F. D'Apuzzo, A. Di Gaspare, I. Lo Vecchio, M. Brahlek, N. Koirala, S. Oh, U. Schade, M. Ortolani, and S. Lupi, Nanoscale **8**, 4667 (2016).

[17] J.-Y. Ou, J.-K. So, G. Adamo, A. Sulaev, L. Wang, and N. I. Zheludev, Nat. Commun. **5**, 5139 (2014).

[18] T. Stauber, J. Phys.: Condens. Matter **26**, 123201 (2014).

[19] V. Marigliano Ramaglia, D. Bercioux, V. Cataudella, G. De Filippis, C. A. Perroni, and F. Ventriglia, Eur. Phys. J. B **36**, 365 (2003).

[20] V. Marigliano Ramaglia, D. Bercioux, V. Cataudella, G. De Filippis, and C. A. Perroni, J. Phys.: Condens. Matter **16**, 9143 (2004).

[21] S. Raghu, S. B. Chung, X.-L. Qi, and S.-C. Zhang, Phys. Rev. Lett. **104**, 116401 (2010).

[22] Y.-P. Lai, I.-T. Lin, K.-H. Wu, and J.-M. Liu, Nanomater. Nanotechnol. **4**, 13 (2014).

[23] D. K. Efimkin, Y. E. Lozovik, and A. A. Sokolik, Nanoscale Res. Lett. **7**, 163 (2012).

[24] D. Kim, S. Cho, N. P. Butch, P. Syers, K. Kirshenbaum, S. Adam, J. Paglione, and M. S. Fuhrer, Nat. Phys. **8**, 459 (2012).

[25] A. N. Grigorenko, M. Polini, and K. S. Novoselov, Nat. Photon. **6**, 749 (2012).

[26] D. Bercioux and P. Lucignano, Rep. Prog. Phys. **78**, 106001 (2015).

[27] V. M. Ramaglia, V. Cataudella, G. De Filippis, and C. A. Perroni, Phys. Rev. B **73**, 155328 (2006).

[28] C. A. Perroni, D. Bercioux, V. Marigliano Ramaglia, and V. Cataudella, J. Phys.: Condens. Matter **19**, 186227 (2007).

[29] G. Siroki, D. K. K. Lee, P. D. Haynes, and V. Giannini, Nat. Commun. **7**, 12375 (2016).

[30] A. Thakur, R. Sachdeva, and A. Agarwal, J. Phys.: Condens. Matter **29**, 105701 (2017).

[31] P. K. Pyatkovskiy, J. Phys.: Condens. Matter **21**, 025506 (2009).

[32] B. Wunsch, T. Stauber, F. Sols, and F. Guinea, New J. Phys. **8**, 318 (2006).

[33] Y. Xia, D. Qian, D. Hsieh, L. Wray, A. Pal, H. Lin, A. Bansil, D. Grauer, Y. S. Hor, R. J. Cava, and M. Z. Hasan, Nat. Phys. **5**, 398 (2009).

[34] C. J. Delerue and M. Lannoo, *Nanostructures - Theory and Modeling* (Springer-Verlag, Berlin, Heidelberg, 2004).

[35] G. Onida, L. Reining, and A. Rubio, Rev. Mod. Phys. **74**, 601 (2002).

[36] F. Bechstedt, *Many-Body Approach to Electronic Excitations - Concepts and Applications* (Springer-Verlag, Berlin, Heidelberg, 2015).

[37] D. Sarid and W. A. Challener, *Modern Introduction to Surface Plasmons. Theory, Mathematica Modeling, and Applications* (Cambridge University Press, Cambridge, 2010)

[38] R. Schütky, C. Ertler, A. Trügler, and U. Hohenester, Phys. Rev. B **88**, 195311 (2013).
[39] M. Li, W. Cui, L. Wu, Q. Meng, Y. Zhu, Y. Zhang, W. Liu, and Z. Ren, Can. J. Phys. **93**, 591 (2015).
[40] P. Sessi, T. Bathon, K. A. Kokh, O. E. Tereshchenko, and M. Bode, Adv. Mater. **28**, 10073 (2016).
[41] P. Ngabonziza, M. P. Stehno, H. Myoren, V. A. Neumann, G. Koster, and A. Brinkman, Adv. Electron. Mater. **2**, 1600157 (2016).
[42] N. Talebi, C. Ozsoy-Keskinbora, H. M. Benia, K. Kern, C. T. Koch, and P. A. van Aken, ACS Nano **10**, 6988 (2016).
[43] F. G. Bassani, V. Cataudella, M. L. Chiofalo, G. de Filippis, G. Iadonisi, and C. A. Perroni, Phys. Status Solidi (b) **237**, 173 (2003).
[44] A. Kogar, S. Vig, A. Thaler, M. H. Wong, Y. Xiao, D. Reig-i-Plessis, G. Y. Cho, T. Valla, Z. Pan, J. Schneeloch, R. Zhong, G. D. Gu, T. L. Hughes, G. J. MacDougall, T.-C. Chiang, and P. Abbamonte, Phys. Rev. Lett. **115**, 257402 (2015).
[45] A. Politano, V. M. Silkin, I. A. Nechaev, M. S. Vitiello, L. Viti, Z. S. Aliev, M. B. Babanly, G. Chiarello, P. M. Echenique, and E. V. Chulkov, Phys. Rev. Lett. **115**, 216802 (2015).
[46] M. Autore, F. D'Apuzzo, A. Di Gaspare, V. Giliberti, O. Limaj, P. Roy, M. Brahlek, N. Koirala, S. Oh, F. J. G. de Abajo, and S. Lupi, Adv. Optical Mater. **3**, 1257 (2015).
[47] C. A. Perroni, V. Cataudella, and G. De Filippis, J. Phys.: Condens. Matter **16**, 1593 (2004).
[48] C. A. Perroni, D. Ninno, and V. Cataudella, New J. Phys. **17**, 083050 (2015).
[49] A. Nocera, C. A. Perroni, V. Marigliano Ramaglia, and V. Cataudella, Phys. Rev. B **86**, 035420 (2012).